Supplementary Information for:

A Carbon Nanotube Optical Reporter Maps Endolysosomal Lipid Flux

Prakrit V. Jena[†1], Daniel Roxbury[†2], Thomas V. Galassi[†1,3], Leila Akkari[1,4], Christopher P. Horoszko[1,3], David B. Iaea[3], Januka Budhathoki-Uprety[1], Nina Pipalia[3], Abigail S. Haka[3], Jackson D. Harvey[1,3], Jeetain Mittal[5], Frederick R. Maxfield[3], Johanna A. Joyce[1,3,6], Daniel A. Heller[1,3*]

[1]Memorial Sloan Kettering Cancer Center, New York, NY 10065

[2]Department of Chemical Engineering, University of Rhode Island, Kingston, RI 02881

[3]Weill Cornell Medicine, New York, NY 10065

[4]Division of Tumor Biology & Immunology, The Netherlands Cancer Institute, Amsterdam, The Netherlands

[5]Department of Chemical and Biomolecular Engineering, Lehigh University, Bethlehem, PA 18015

[6]Ludwig Center for Cancer Research, University of Lausanne, Switzerland, CH 1066

† Contributed equally to this work

* Corresponding author. Email: hellerd@mskcc.org

KEYWORDS: single-walled carbon nanotubes, single-cell sensing, live-cell imaging, near-infrared fluorescence, hyperspectral microscopy

Table of Contents

Supplementary Figures and Text:

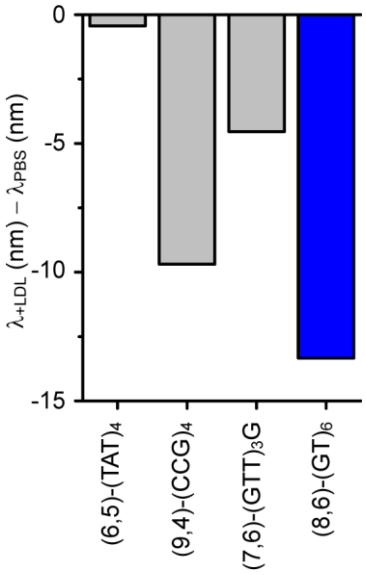

Figure S1: Photoluminescence wavelength response of DNA-nanotube complexes to low density lipoprotein (LDL). Response of nanotube emission to 0.5 mg/mL LDL in solution after an18 hour incubation time.

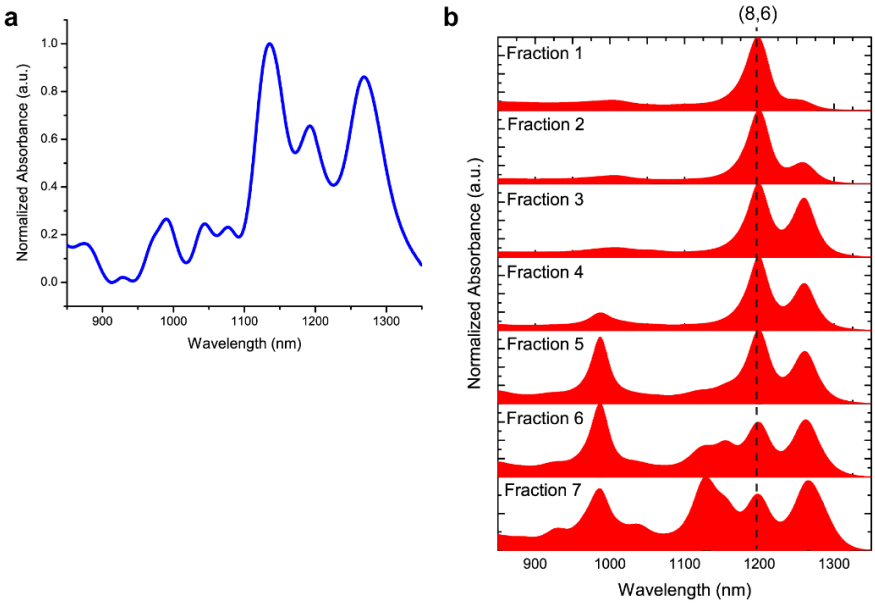

Figure S2: Ion exchange (IEX) chromatographic separation of the (8,6) chirality from ss$(GT)_6$-SWCNT complexes. **a)** Absorbance spectrum of unsorted ss$(GT)_6$-SWCNT (HiPco) complexes. **b)** Absorbance spectra of eluted fractions of ss$(GT)_6$-SWCNT complexes after passing through an anion exchange column.

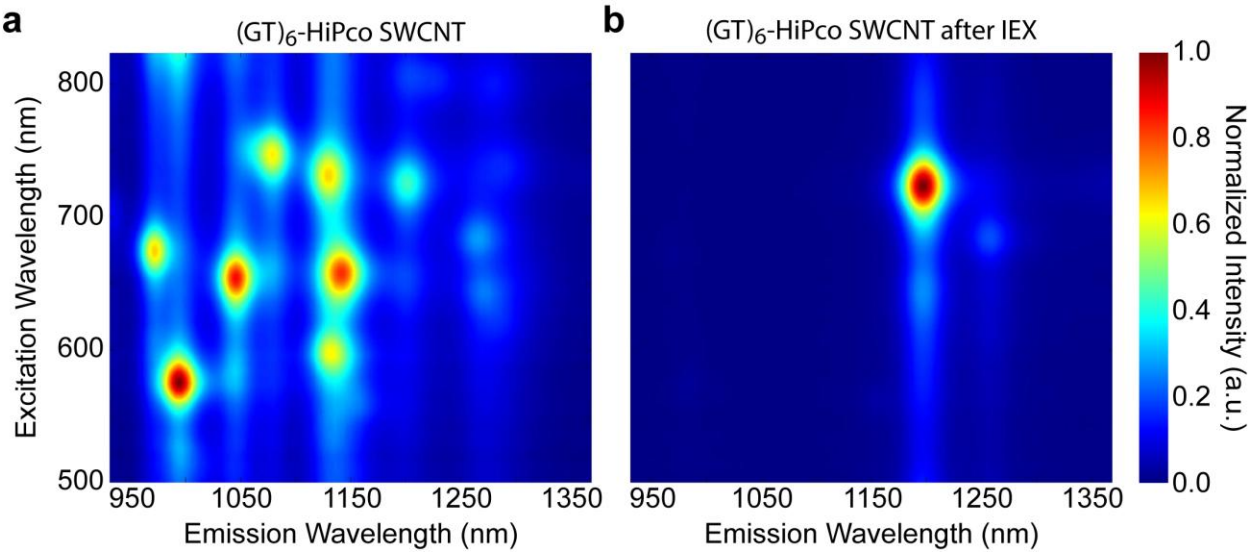

Figure S3: Two-dimensional photoluminescence excitation/emission contour maps (PL plots) of unsorted and ion exchange-purified ss$(GT)_6$-SWCNT complexes in solution. **a)** PL plot of unsorted HiPco carbon nanotubes dispersed using a DNA oligonucleotide with the sequence ss$(GT)_6$. **b)** PL plot of ss$(GT)_6$-(8,6) nanotube complexes purified by ion exchange chromatography (IEX).

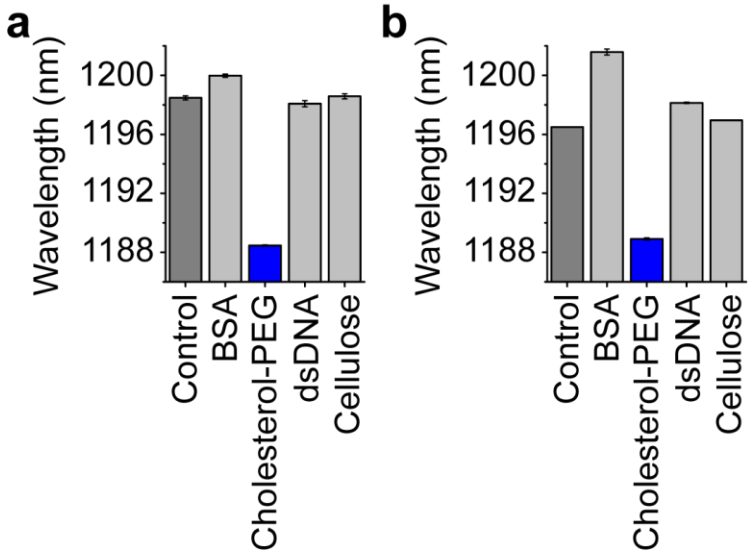

Figure S4: Specificity of the ss$(GT)_6$-(8,6) optical response to lipids. Nanotube emission center wavelength in solution at saturating concentrations of BSA (40 mg/mL), cholesterol-PEG (30 mg/mL), salmon testes dsDNA (2 mg/mL), and carboxymethyl cellulose (CMC, 10 mg/mL) at both **(a)** 2 and **(b)** 24 hours after addition. All error bars represent standard deviation from n = 3 technical replicates.

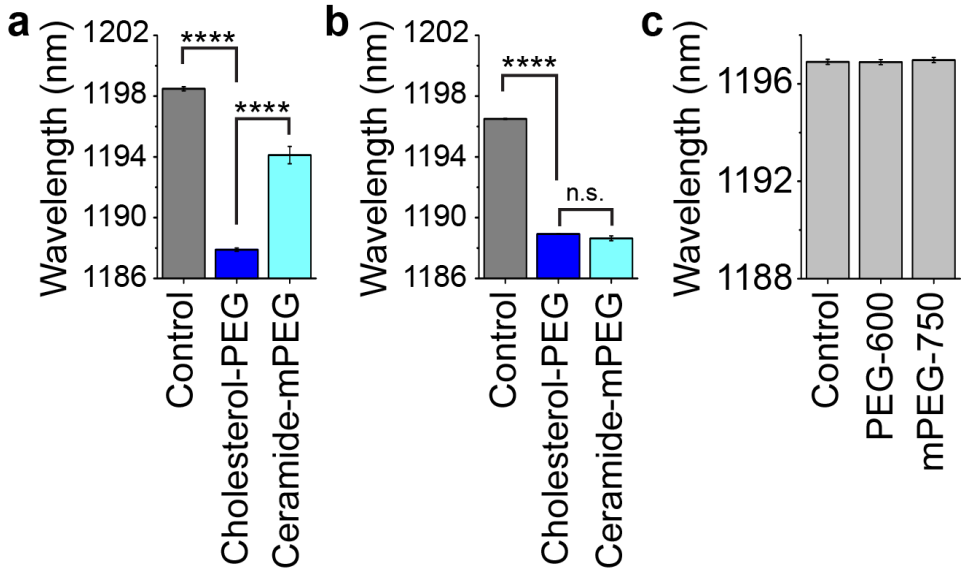

Figure S5: General optical response of ss$(GT)_6$-(8,6) to lipids. **a)** Nanotube emission center wavelength in solution at 5 μM concentrations of PEG (OH-terminated) or methoxy PEG (mPEG)-conjugated lipid analogs 2 hours after introduction and **b)** upon 6 hours of incubation. **c)** Nanotube emission center wavelengths in response to 5 μM of PEG with molecular weights matching those from the lipid analogs. All error bars represent standard error of the mean from n = 3 technical replicates. Values were compared using a one way ANOVA with Sidak's multiple comparison test, **** = $p < 0.0001$.

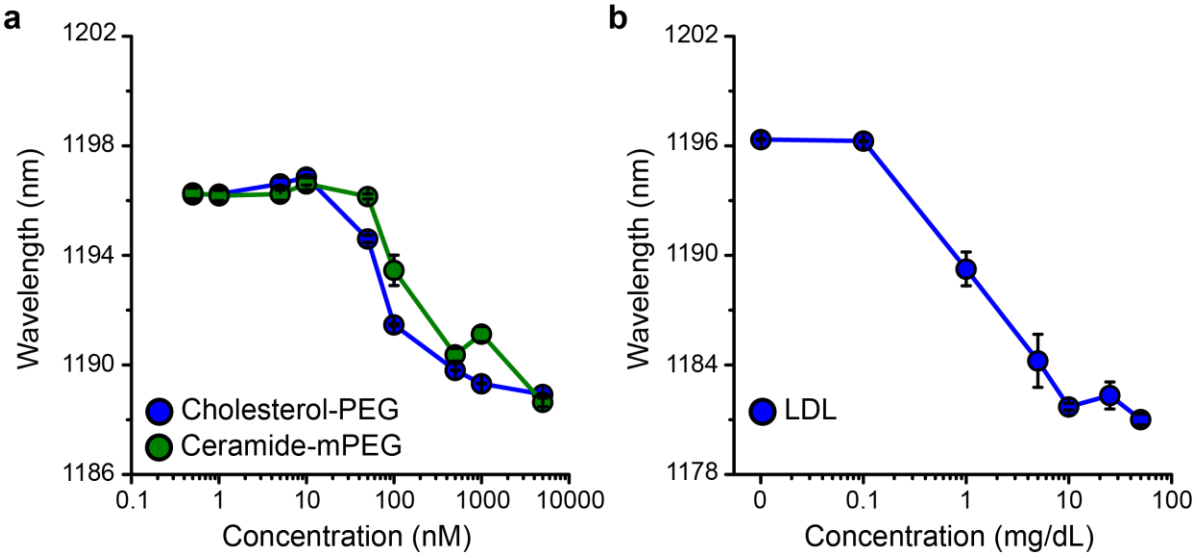

Figure S6: Concentration curves of the response of the ss$(GT)_6$-(8,6) complex to lipids. **a**) Response 24 hours after the addition of water-soluble lipid analogs. **b)** Response 24 hours after the addition of low-density lipoprotein (LDL). Error bars are standard errors of the mean, from n = 3 technical replicates.

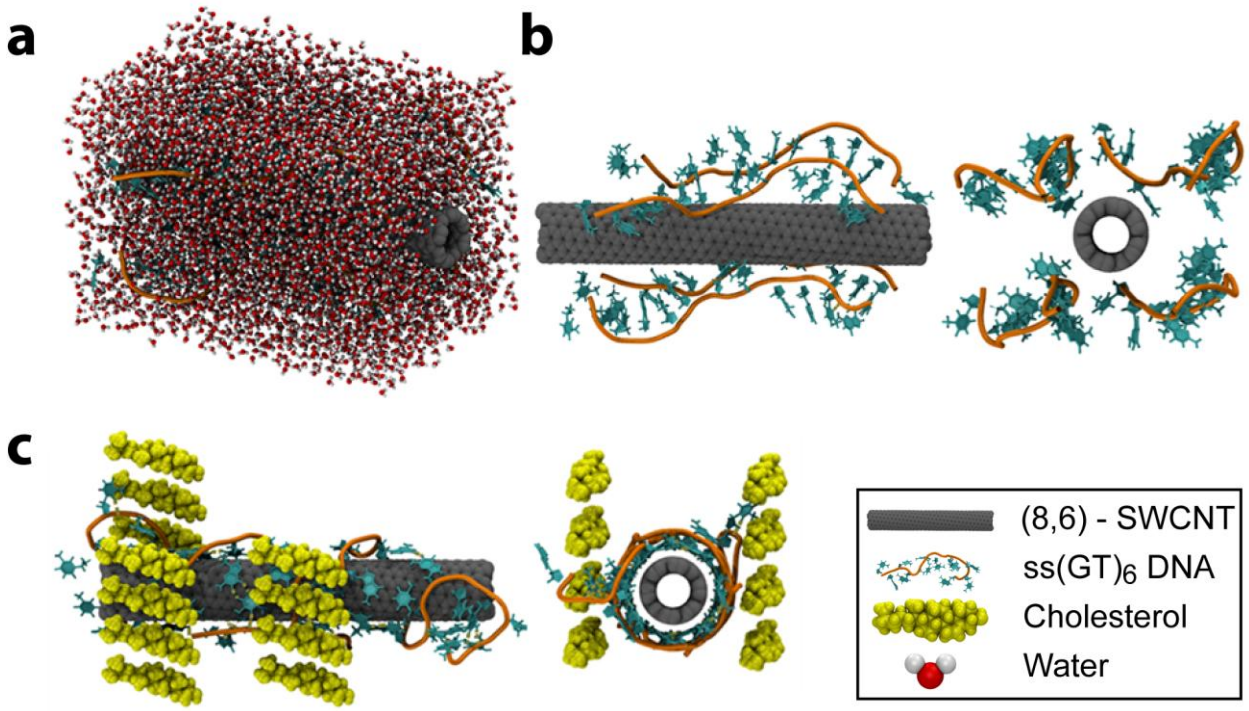

Figure S7: Initial replica exchange molecular dynamics (REMD) configurations of ss$(GT)_6$-(8,6) with cholesterol. The same starting configurations were also used for sphingomyelin simulations, with sphingomyelin molecules replacing cholesterol molecules. **a)** Starting configuration of the ss$(GT)_6$ DNA oligonucleotide with the (8,6) nanotube species shown in a water box with counter-ions. **b)** Side and end-on views of ss$(GT)_6$ + (8,6) nanotube shown with water and ions removed. **c)** Side and end-on view of the ss$(GT)_6$-(8,6) nanotube complex in the presence of cholesterol.

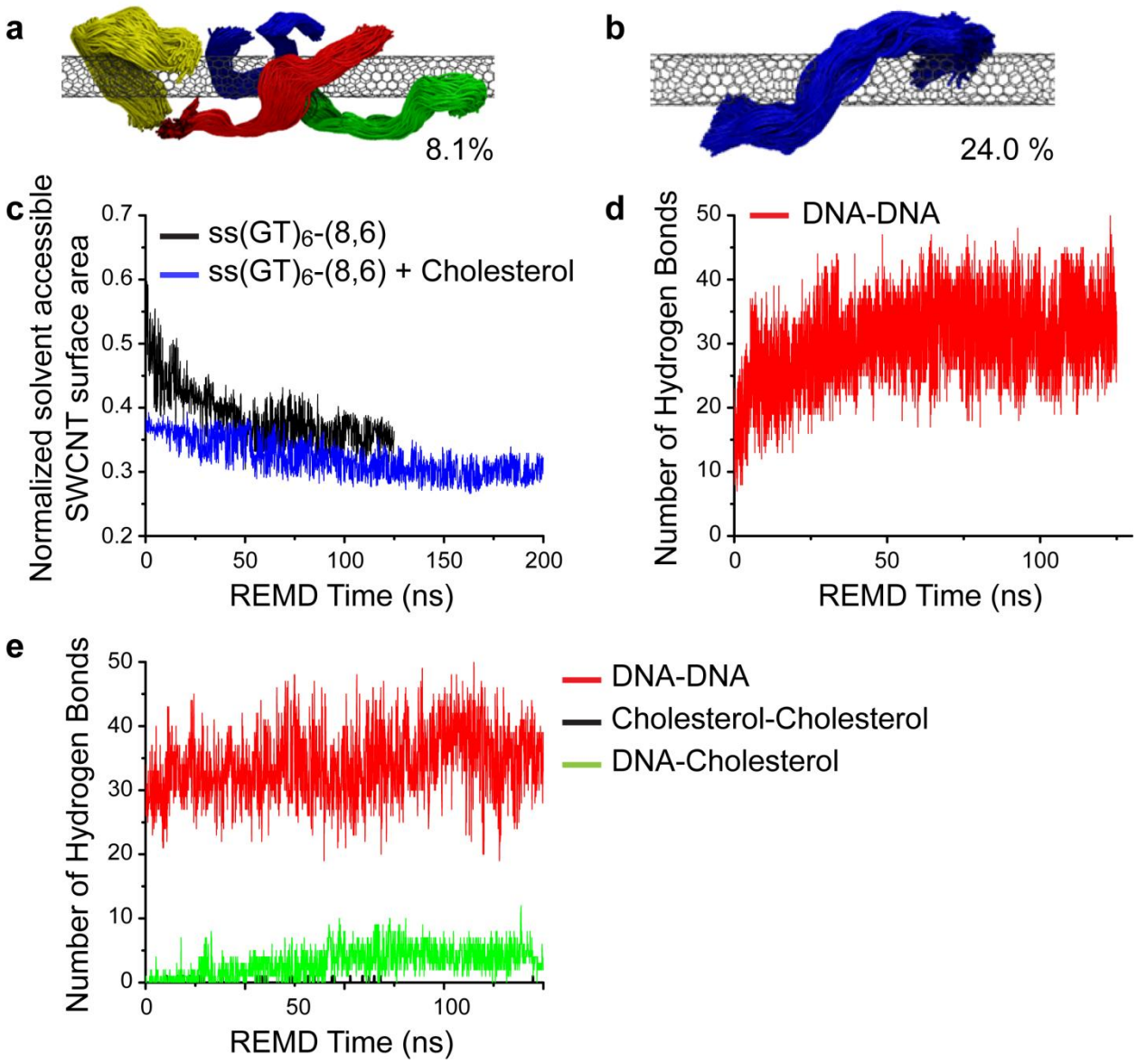

Figure S8: Analysis of REMD simulations of ss$(GT)_6$-(8,6) with cholesterol. **a)** Top cluster for the ss$(GT)_6$ + (8,6) configuration based on root mean square deviation (RMSD) of all DNA backbone atoms, where each color represents a different strand. This structure represents 8.1% of the production trajectory. **b)** Top cluster for the same configuration based on DNA backbone atoms of a single strand. This structure represents 33.0% of the trajectory. **c)** Solvent accessible SWCNT surface area vs. simulation time for the two simulated configurations (with and without cholesterol). **d)** Number of hydrogen bonds between DNA strands vs. simulation time for the ss$(GT)_6$ + (8,6) configuration. **e)** Number of hydrogen bonds formed between DNA strands, cholesterol molecules, and DNA-cholesterol vs. simulation time for the ss$(GT)_6$ + (8,6) + cholesterol configuration

Molecular dynamics simulations

All-atom replica exchange molecular dynamics (REMD) simulations[1-3] were performed to understand the interactions between a carbon nanotube, single-stranded DNA, cholesterol, and sphingomyelin. Four strands of ss$(GT)_6$ DNA were placed in a desorbed state in the vicinity of a 7.527 nm long SWCNT with an (8,6) chirality. The DNA and SWCNT were solvated in a 5 x 5 x 7.527 nm water-box containing approximately 5,000 TIP3P model[4] water molecules and sodium counter-ions, placed randomly, to balance the negative charges from phosphates on DNA (Figure S7a, b). The total system was ~18,000 atoms. The SWCNT extended to the edge of the water box. The SWCNT atoms were modeled as sp^2 hybridized carbon. All structures were visualized in VMD.[5]

To run the REMD simulations, the Gromacs 4.6.7 simulation package was used with the Charmm36 force field. Long-range electrostatics were calculated using the particle mesh Ewald method with a 0.9 nm real space cutoff. For van der Waals interactions, a cutoff value of 1.2 nm was used. The DNA-SWCNT configuration was energy minimized and subjected to 100 ps equilibration (NVT) at 300 K. Forty replicas were created with temperatures ranging from 300 K to 585 K. Temperature intervals increased with absolute temperature to maintain uniform exchange probability. The 40 replicas were run in parallel for 125 ns of NVT production. Exchange between adjacent temperature replicas was attempted every 2 ps and the temperature list was optimized to ensure that the acceptance ratio remained at least 20%. The time step of the simulation was 2 fs. The trajectories were saved every 10 ps, yielding a total of 12,500 snapshots for production analysis. For clustering, solvent accessibility, water density, and hydrogen bonding analysis, the 300 K trajectory was used.

Twelve molecules of cholesterol or six molecules of sphingomyelin were evenly distributed in the water-box of the top equilibrium cluster of the ss$(GT)_6$ + (8,6) configuration (Figure S7c). This configuration served at the initial configuration for the combination simulation (DNA + cholesterol). The system was again energy-minimized, heated to 100 ps (NVT), and replicated in temperature space. The configuration was then run for 200 ns of NVT production. Again, the 300 K trajectory was used for subsequent analysis. The simulation time totaled ([125 ns x 40] + [200 ns x 40]) = 13 μs.

Clustering of the REMD trajectory is useful to determine the underlying equilibrium structures in the simulated configuration. Here, we used a native Gromacs clustering function (g_cluster) with a root mean square deviation **(**RMSD) cutoff of 0.8 nm based upon the positions of the DNA backbone atoms. The top cluster from the 12,500 available snapshots (Figure S8a) represented 8.1% of the total 300 K trajectory. We found significant inter-strand and intra-strand DNA interactions in the top cluster. In agreement with previous studies,[1,2] the DNA remained bound to the SWCNT throughout the duration of the simulation. To probe the behavior of any single strand of DNA, clustering was performed using the atom positions of a single strand of DNA (Figure S8b). This structure represented a significantly higher portion of the trajectory, indicating that any single strand preferentially adopted a left-handed helical wrapping around the nanotube.

The solvent accessibility was analyzed using the Gromacs function 'g_sas'. In the ss$(GT)_6$ + (8,6) configuration, it was clear that the DNA evolved to wrap the SWCNT, from its initially unbound state, and shield the SWCNT from solvent (water or sodium) molecules (Figure S7c).

The addition of the cholesterol molecules in the subsequent simulation further decreased the solvent accessibility to the SWCNT surface. Although the solvent accessibility to surface molecules decreased, there was a large change in water density. This reflects the hydrophobic nature of cholesterol-water interface rather than steric constraint. This data is in agreement with a decrease in water density found near the surface of the SWCNT in the ss$(GT)_6$ + cholesterol or sphingomyelin + (8,6) configuration (Figure 1d, e).

Hydrogen bonding analysis was performed using the Gromacs function 'g_hbond'. In the ss$(GT)_6$ + (8,6) configuration, there was a significant increase in the number of DNA-DNA hydrogen bonds as the DNA adsorbed onto the SWCNT and adopted an equilibrium arrangement (Figure S8d). It was clear that between 0-50 ns of REMD time, the number of hydrogen bonds was still increasing to its equilibrium value of 32.6 ± 5.2, and could be discarded as initial equilibration data. When cholesterol was introduced to the ss$(GT)_6$ + (8,6) configuration, there was an evolution over a time period of ~125 ns in which the number of DNA-cholesterol hydrogen bonds increased to an average value of 4.2 ± 1.8, while the number of DNA-DNA hydrogen bonds remained relatively unchanged (Figure S8e).

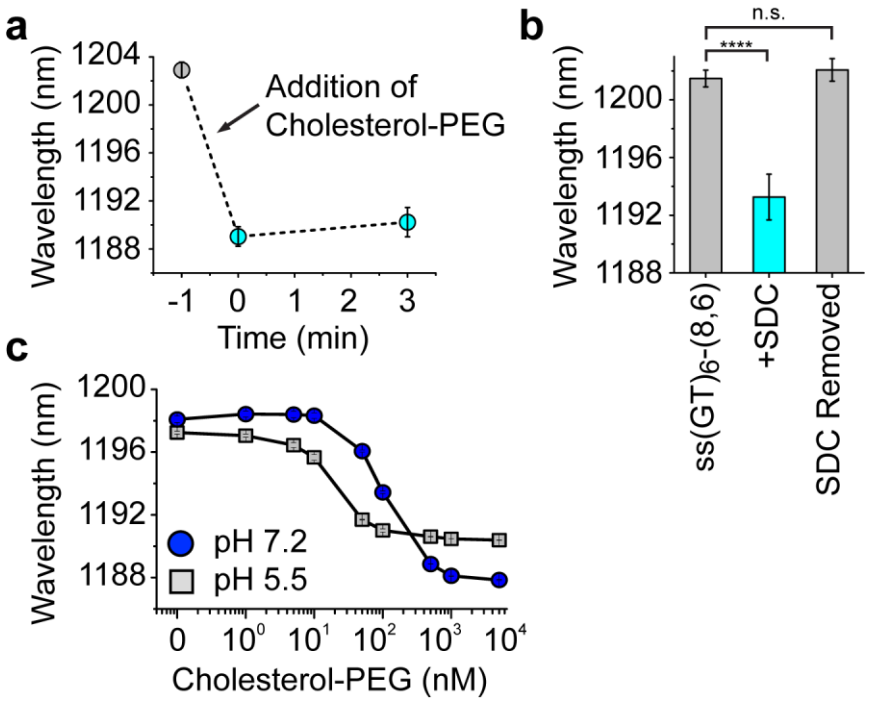

Figure S9: Characterization of the ss$(GT)_6$-(8,6) optical response. **a)** The emission from surface-adsorbed ss$(GT)_6$-(8,6) complexes acquired as a function of time after addition of 30 mg/mL of cholesterol-PEG. Error bars are standard error of the mean at each time point, from n = 80 individual nanotubes. **b)** The emission wavelength of complexes bound to a glass surface, upon addition of 1% sodium deoxycholate (SDC), and after SDC was rinsed away with saline buffer. Error bars are standard error from the mean, and emission was compared using a one-way ANOVA with Dunnett's multiple comparisons test for n = 4 technical replicates. All error bars represent standard error of the mean. **** = $p < 0.0001$. **c)** The nanotube complex emission in solution measured as a function of cholesterol-PEG concentration at pH 7.2 and pH 5.5. Error bars are standard deviations from n = 3 technical replicates.

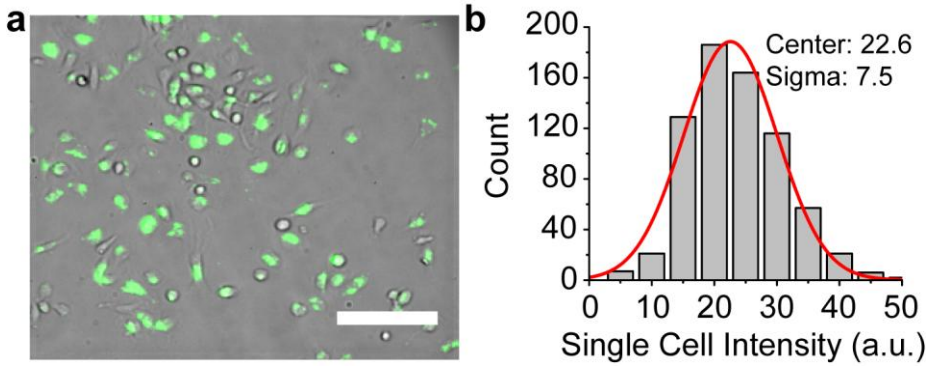

Figure S10: Uptake of ss$(GT)_6$-(8,6) complexes in live cells. **a)** Overlay of near-infrared emission from the complexes over the transmitted light image from a field of bone marrow-derived macrophages. **b)** Histogram of the mean intensity from individual cells, obtained from over 700 cells, and a Gaussian fit of the histogram, bin size = 5 nm. Scale bar = 100 µm.

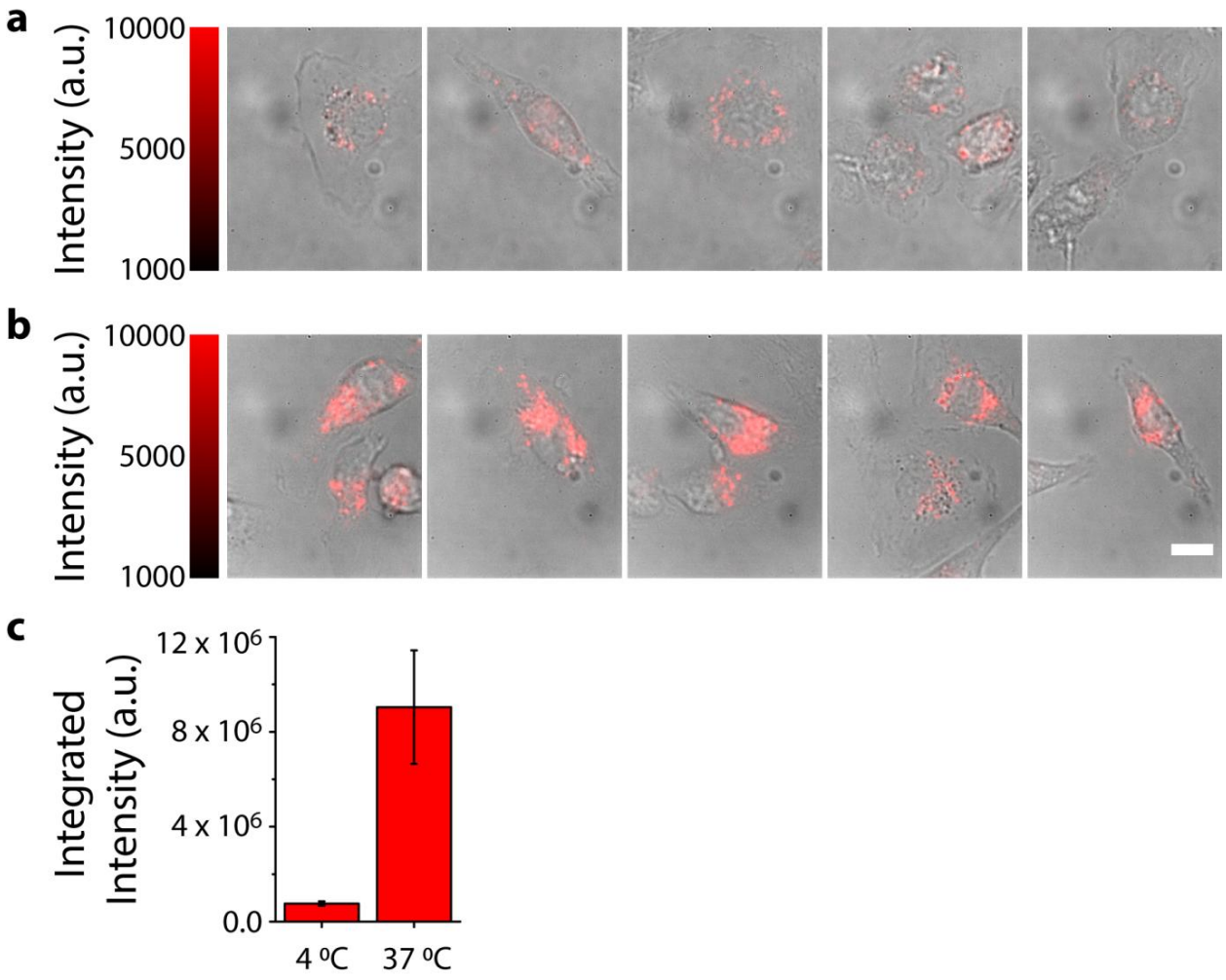

Figure S11: Uptake of ss$(GT)_6$-(8,6) complexes upon incubation at 4 °C and 37 °C with live cells. Overlays of transmitted light images and near-infrared emission from the complexes at **a)** 4 °C and **b)** 37 °C, displayed at the same intensity scale. The bone marrow-derived macrophages (differentiated for 3 days with CSF-1) were incubated in complete media containing the complex for 30 minutes. The cells were washed to remove cell surface-adsorbed complexes and then incubated for 6 hours in the complex-free media prior to imaging. **c)** Bar graph comparing the integrated nanotube emission intensities from each condition. Scale bar = 10 µm. Error bars are standard errors of the mean from n = 10 fields of view for each condition.

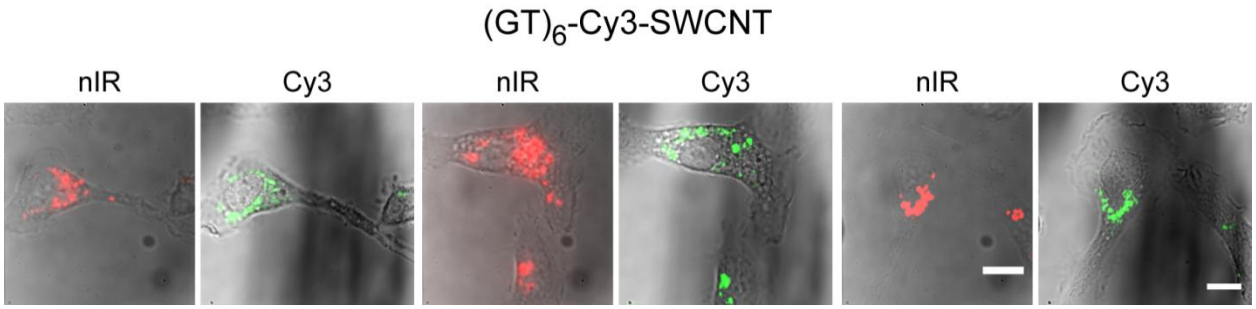

Figure S12: Visible and near-infrared (nIR) imaging of Cy3-ss$(GT)_6$-nanotube complexes in live cells. Cy3-labeled ss$(GT)_6$ DNA-nanotube complexes were incubated for 30 minutes with maturing bone marrow-derived cells (after 3 days of CSF-1 treatment). Upon washing away unbound complexes from the solution, the cells were imaged in fresh media. The nIR channel (red) is the broadband 900-1650 nm emission from complexes inside the cells, collected using a 2D nIR InGaAs array camera following 730 nm laser excitation of the sample. The Cy3 channel (green) shows epifluorescence using a standard 120-watt lamp light source, a 545/620 nm filter set (Chroma 41002C), and CCD camera. Micrographs from both images were overlaid onto transmitted light images acquired with the respective cameras. Scale bars are 10 μm and apply to all images from the same channel.

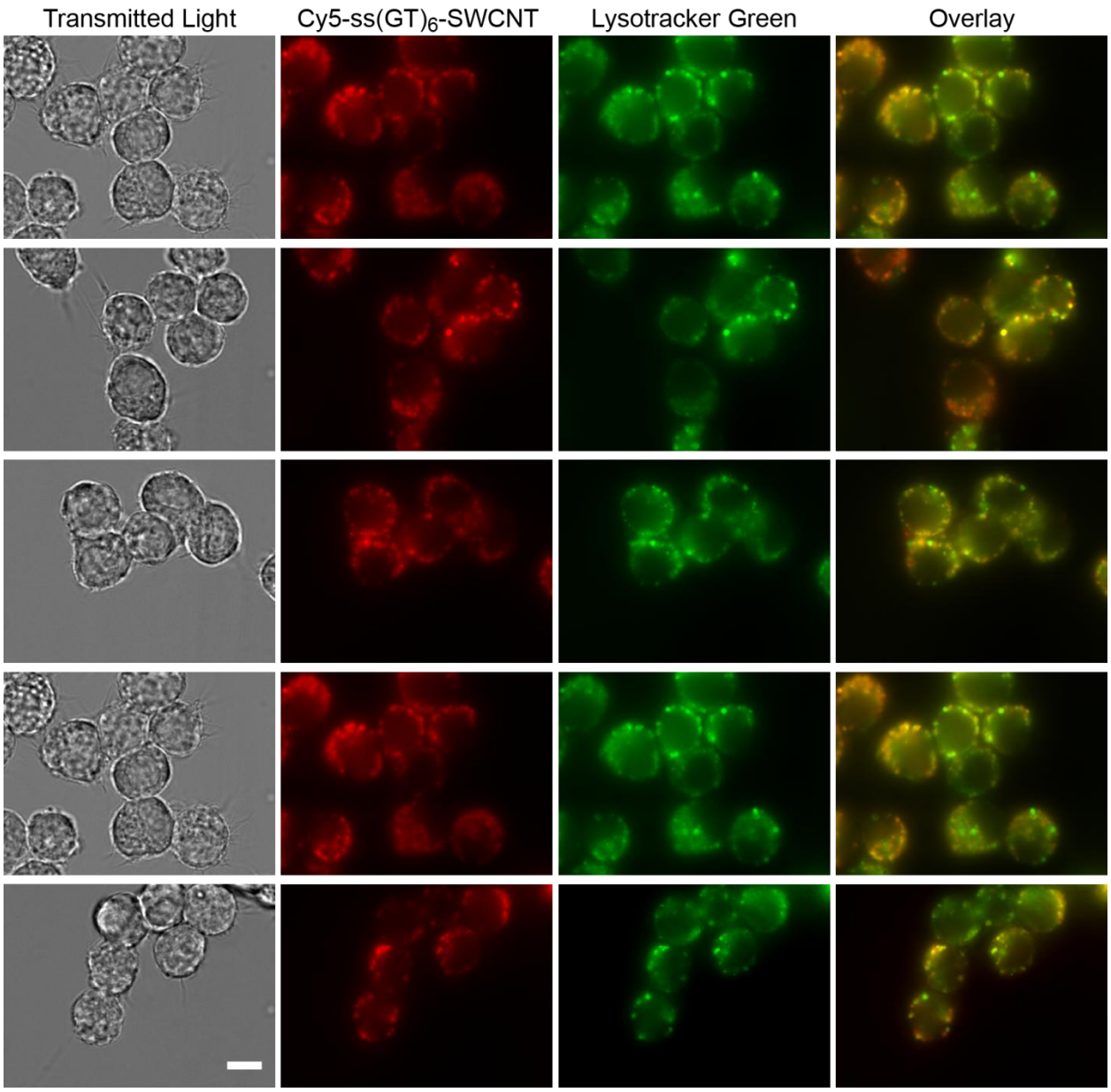

Figure S13: Fluorescence microscopy of DNA-nanotube complexes and Lysotracker in live cells. Cy5-labeled ss$(GT)_6$-nanotube complexes (1 mg/L incubated for 30 minutes at 37° C) in RAW 264.7 macrophages stained with Lysotracker Green. The Cy5 emission (red) was imaged using a 620/700 nm (Chroma 49006) filter set and Lysotracker Green emission (green) was imaged using a 545/620 nm filter set (Chroma 41002C). The overlaid channel appears as yellow where signals are colocalized. The background-subtracted images were thresholded using an unbiased method developed by Costes *et al.*,[6] and colocalization was performed on 10 independent fields of view. Scale bar = 10 μm.

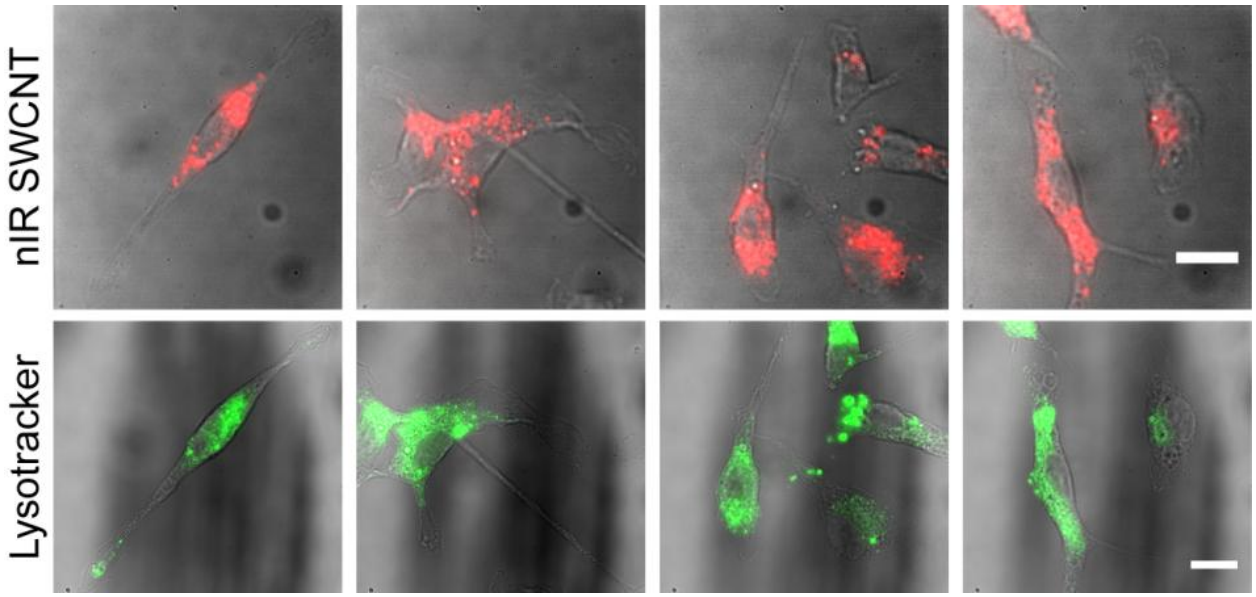

Figure S14: Images of NIR emission from ss$(GT)_6$-(8,6) complexes and visible emission from Lysotracker in fixed cells. The ss$(GT)_6$-(8,6) complexes were incubated with bone-marrow-derived macrophages and fixed before incubating with Lysotracker Deep Red stain. (Red) Transmitted light and near-infrared (nIR) emission overlay. (Green) Transmitted light and Lysotracker Deep Red overlay, which was imaged using a 620/700 nm (Chroma 49006) filter set. Two different cameras (InGaAs and CCD) were used to acquire the images. Scale bars = 10 μm.

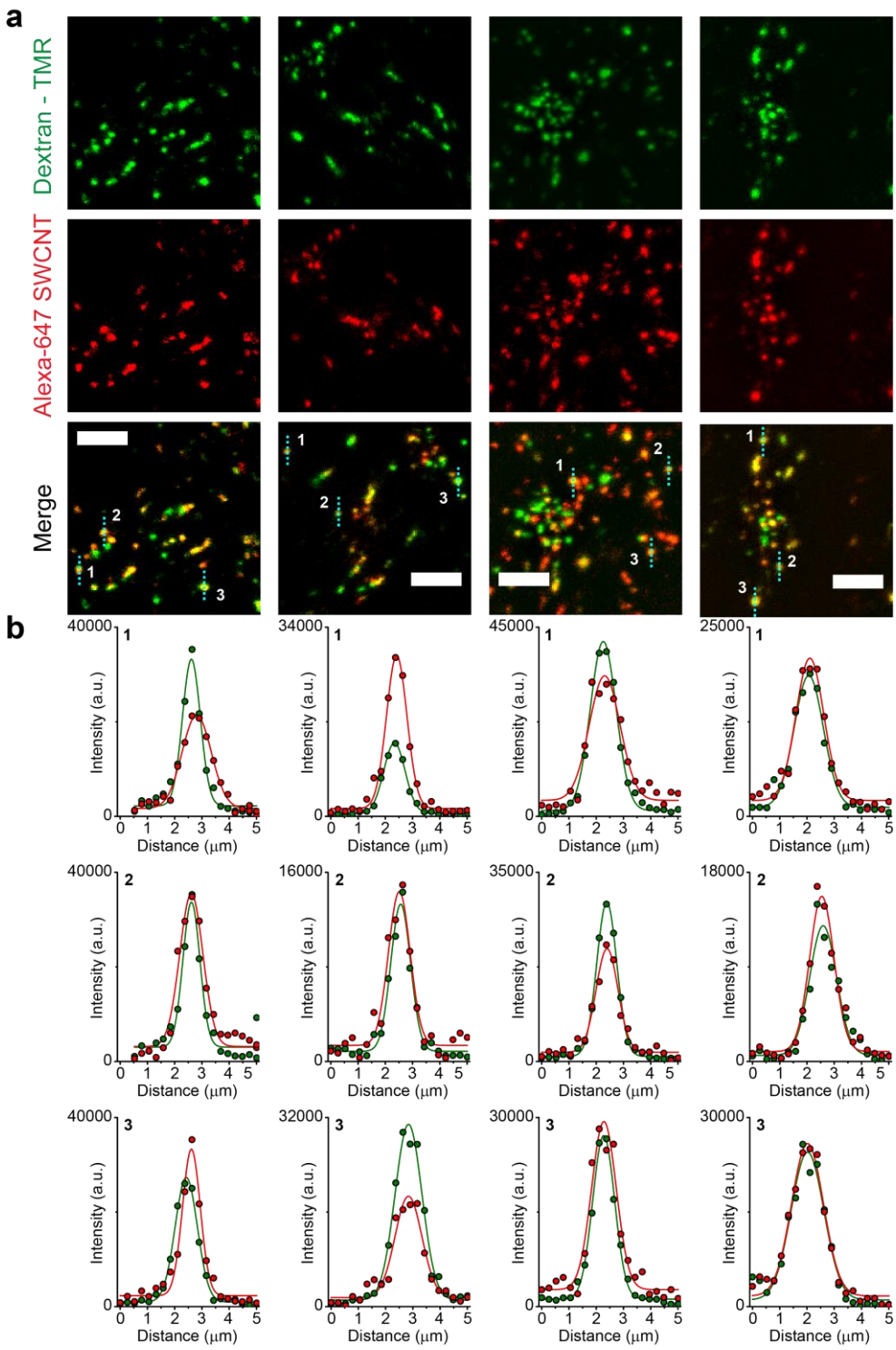

Figure S15: Confocal imaging of TMR-dextran and Alexa-647-nanotubes in U2OS-SRA cells. **a)** TMR-labeled dextran (green), Alexa 647-labeled SWCNT (red), and merged overlay images. Lines (cyan) denote cross sections from the images extracted for further analysis. Scale bars = 10 μm. **b)** Intensity profiles of TMR (green) and Alexa 647 (red) fit with Gaussian functions.

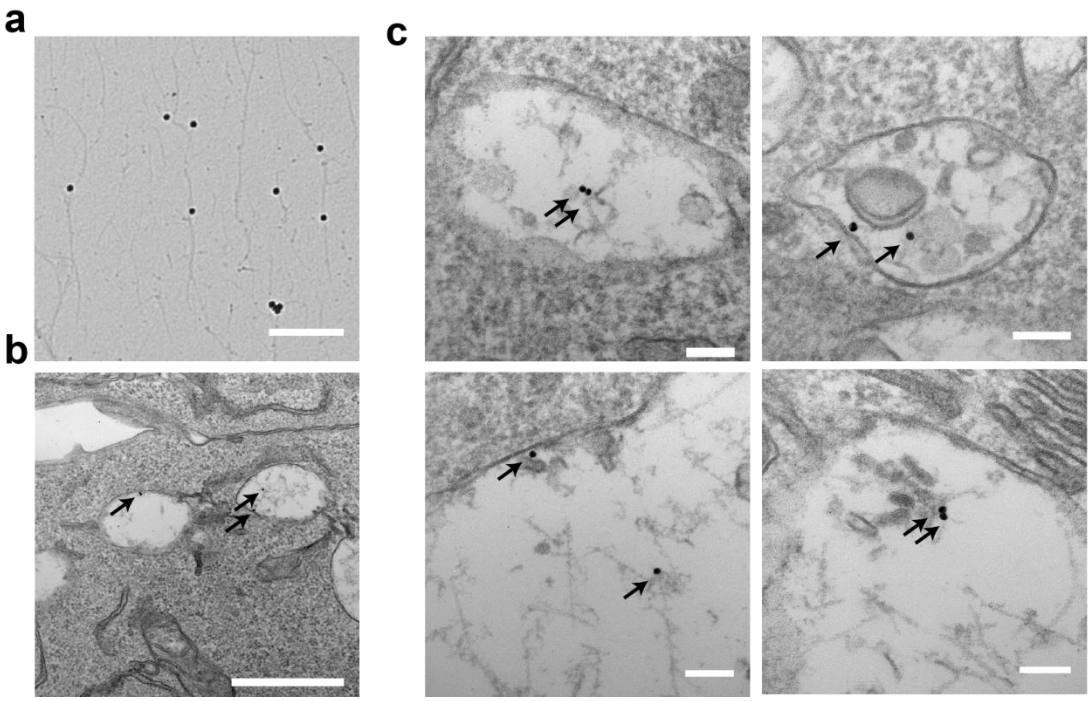

Figure S16: TEM images of gold nanoparticle-SWCNT (AuNP-SWCNT) complexes in RAW 264.7 macrophages. **a)** AuNP-SWCNT complexes imaged on the TEM grid. Scale bar = 250 nm. **b)** Representative TEM image of macrophages incubated with AuNP-SWCNT complexes. Scale bar is 1 µm. **c)** Representative high-magnification images of AuNP-SWCNT complexes within endolysosomal organelles. Scale bars are 100 nm. Arrows point to the AuNPs.

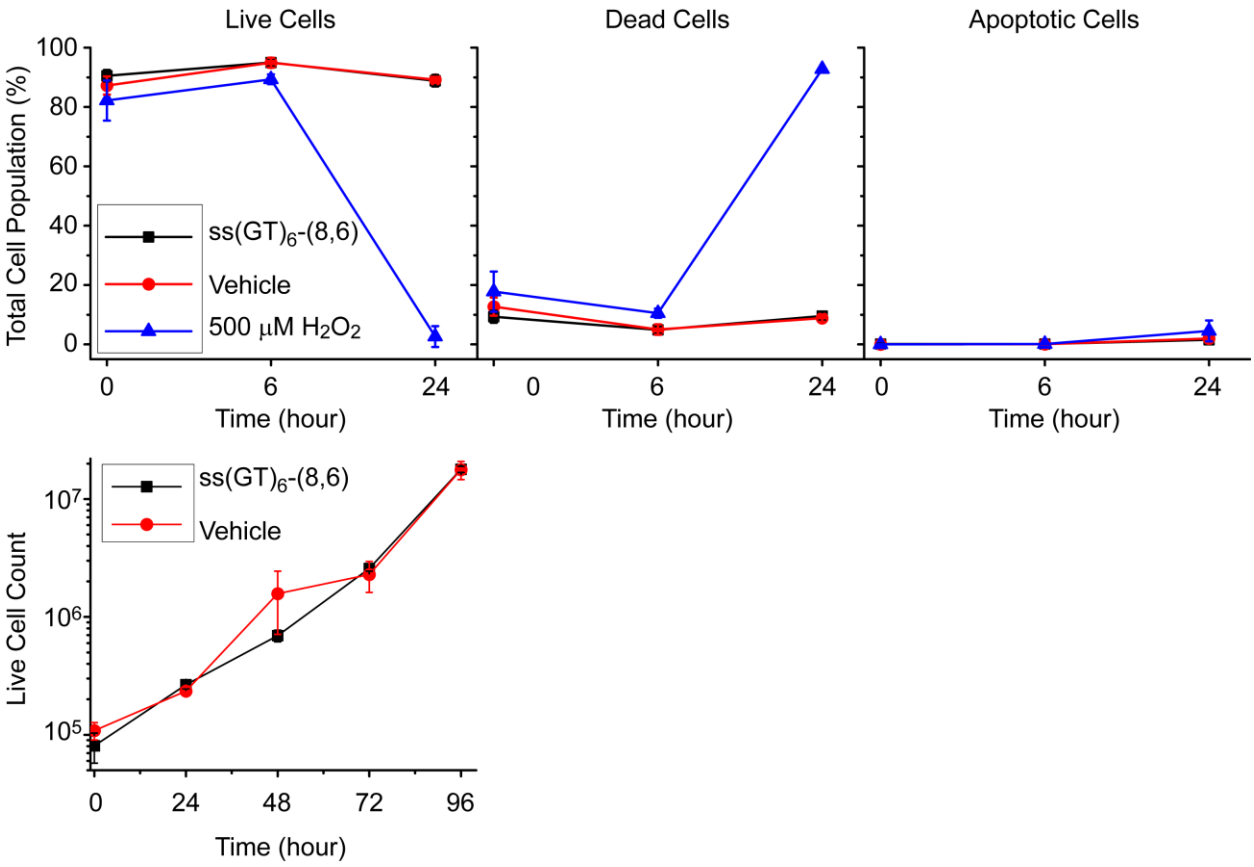

Figure S17: Viability and proliferation assays conducted on cells exposed to ss(GT)$_6$-(8,6) complexes. The complexes were introduced to RAW 264.7 macrophages in standard culture conditions at 0.2 mg/L for 30 minutes before replacing with fresh media. **a)** Cell viability and apoptosis assays, measured *via* annexin V and propidium iodide. 500 μM H_2O_2 was used as a positive control for cell death. **b)** Cell proliferation assay, reported as the number of living cells *versus* time. Error bars denote standard error of the mean, n = 3 technical replicates.

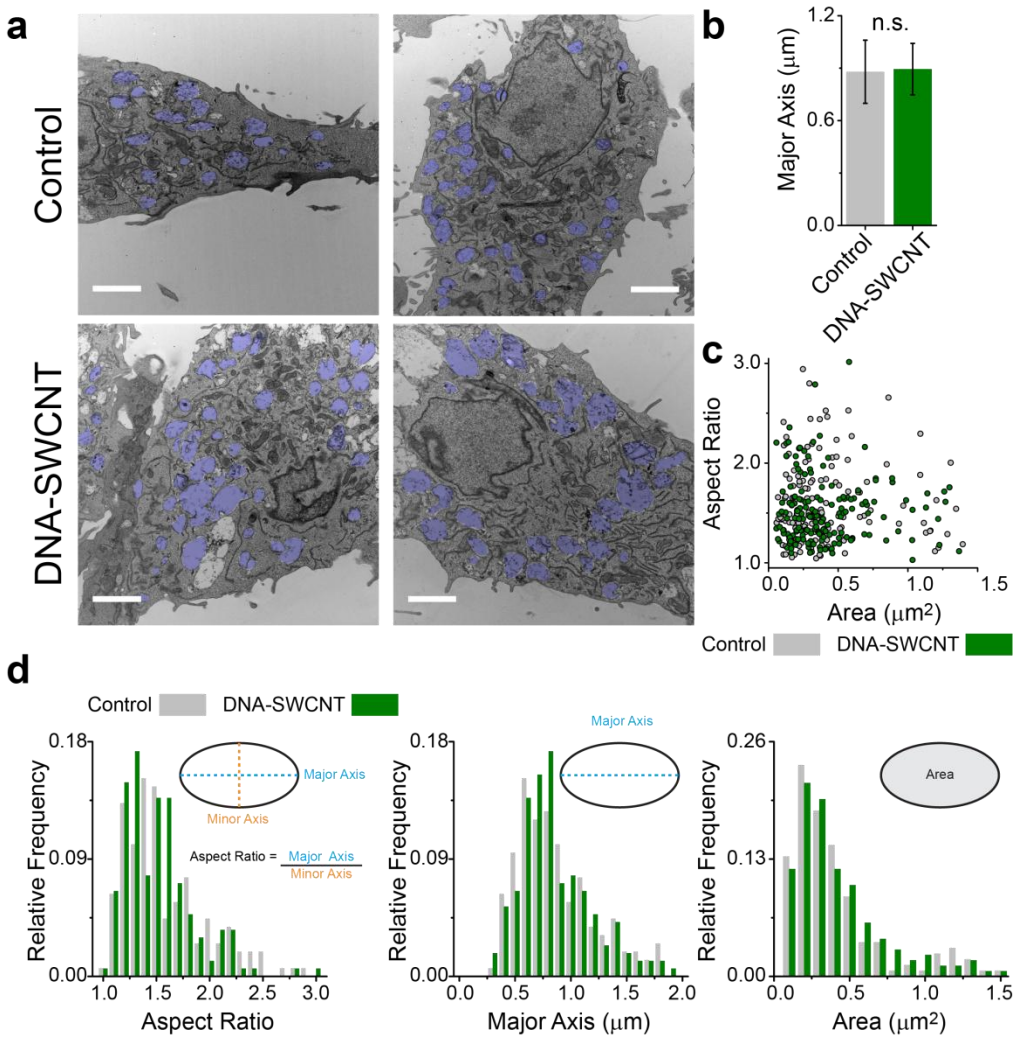

Figure S18: Structural morphology analysis of endolysosomal organelles in RAW 264.7 macrophages using TEM. **a)** Endolysosomal organelles (shaded blue) from cells incubated with 1 mg/L of gold nanoparticle-nanotube complexes, and untreated cells. Scale bars are 2 μm. **b)** Comparison of the mean major axis length of the endolysosomal organelles in nanotube-treated and untreated cells. Error bars are standard deviations. Mean values were compared using an unpaired t-test. **c)** Scatter plot of aspect ratio vs. area of each endolysosomal organelle. **d)** Histograms of the aspect ratio, major axis diameter, and area of at least 150 endolysosomal organelles for each condition.

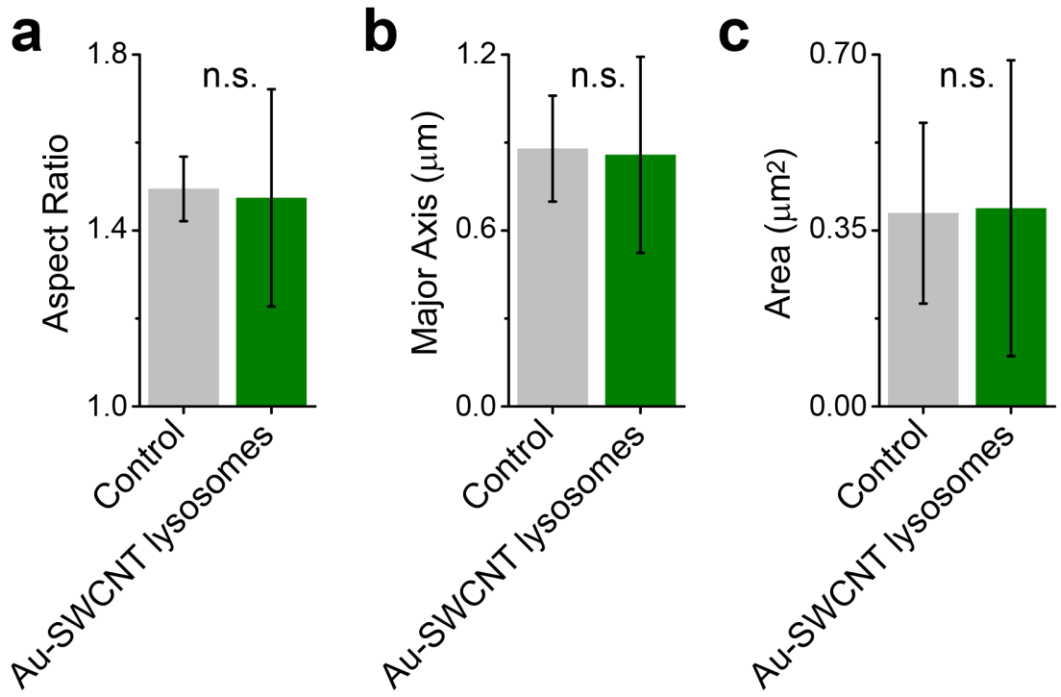

Figure S19: Structural morphology analysis of TEM images of endolysosomal organelles in RAW 264.7 macrophages incubated with 1 mg/L gold nanoparticle-nanotube complexes. **(a)** Comparison of the mean aspect ratio of endolysosomal organelles containing AuNPs to those in control cells. **(b)** Comparison of the mean major axis length of endolysosomal organelles containing AuNPs to those in control cells. **(c)** Comparison of the mean area of endolysosomal organelles containing AuNPs to those in control cells. All error bars are standard deviations. Mean values were compared using an unpaired t-test.

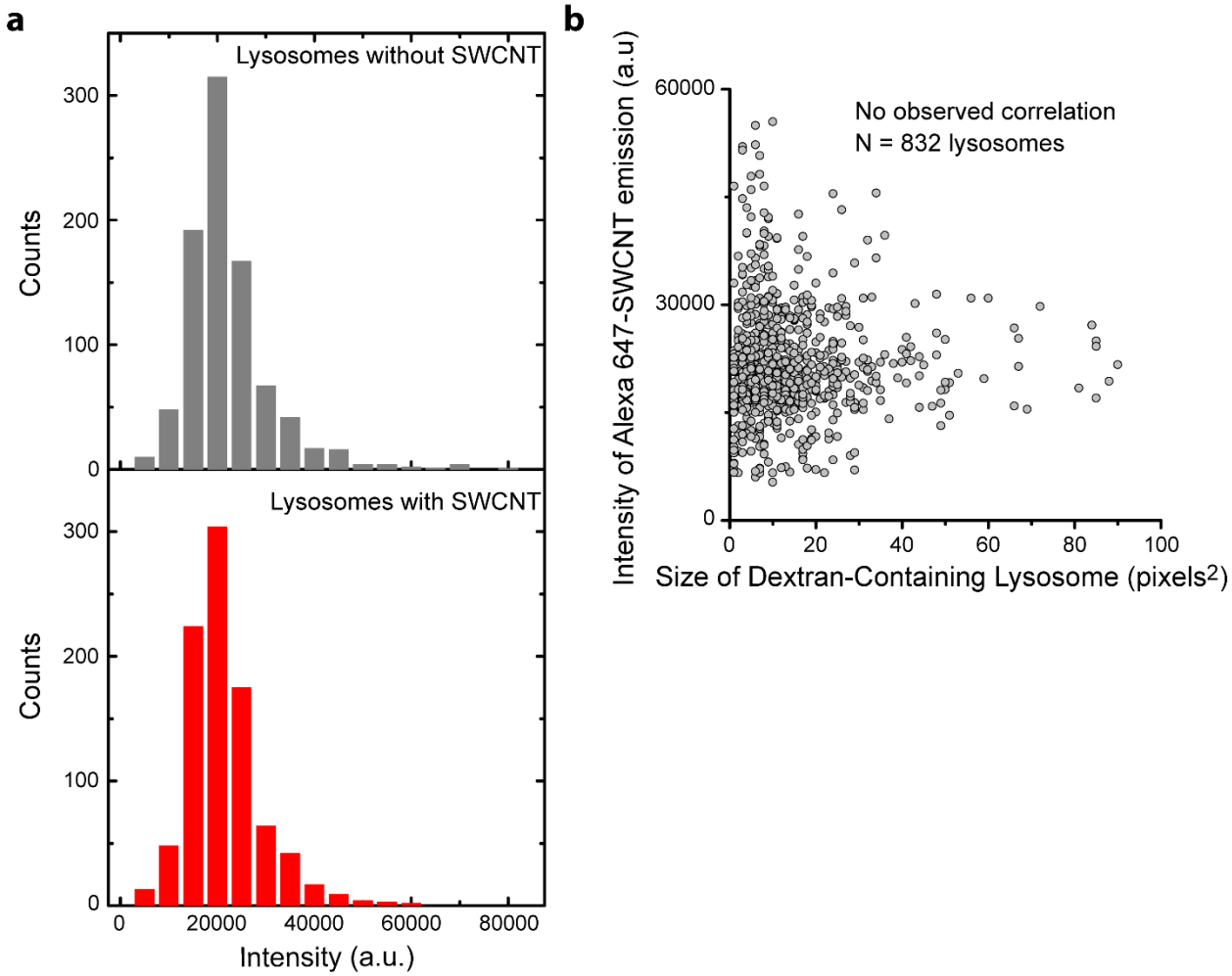

Figure S20: Assessments of contents and size of endolysosomal organelles in U2OS-SRA cells in the presence of nanotubes. **a)** Histograms of the TMR-dextran intensity from endolysosomal organelles in cells containing nanotubes and untreated cells. **b)** Scatter plot of the areas of TMR-dextran-illuminated endolysosomal organelles vs. Alexa 647-SWCNT emission from the same organelles.

<u>Assessment of the effects of DNA-SWCNT on endolysosomal integrity</u>

U2OS-SRA cells incubated overnight with 10,000 MW dextran labeled with TMR, were then maintained in dextran-free media for 3 hours. Alexa-647 labeled nanotube complexes were then introduced to the cell media for 30 minutes. After washing away free complexes, high magnification confocal microscopy in the live cells was performed and we quantitatively analyzed the intensity distributions of TMR-dextran and Alexa 647-SWCNT in endolysosomal organelles. Histograms of TMR-dextran intensity in cells containing nanotubes and control cells (Figure S20a) showed no decrease in the dextran content of lysosomes in the presence of nanotubes. This data suggest that the nanotubes did not induce lysosomal membrane permeabilization, wherein dextran leakage would be evident.

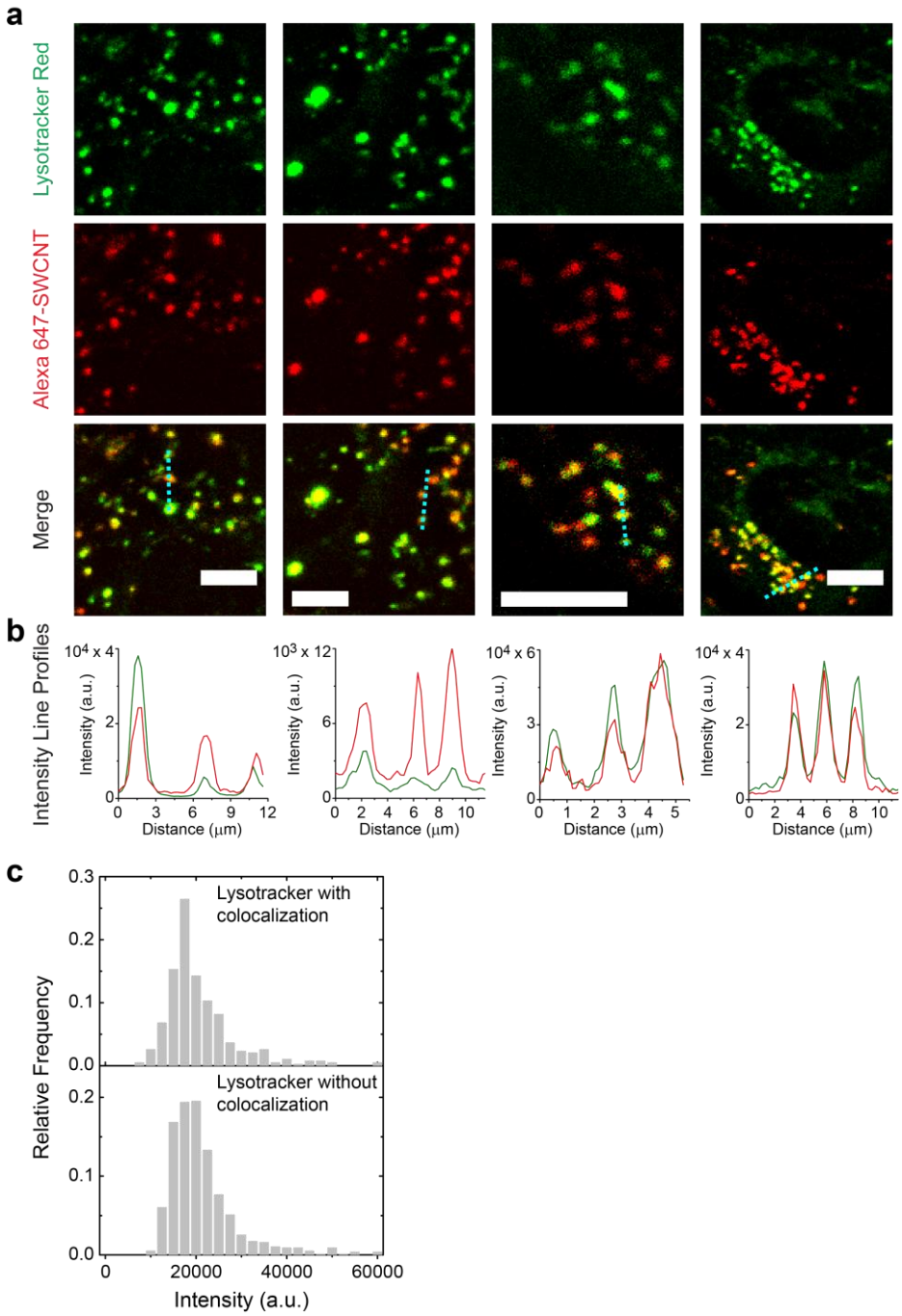

Figure S21: Confocal imaging study of Lysotracker Red and Alexa-647-DNA-nanotube complexes in U2OS-SRA cells. **a)** Lysotracker Red (green), Alexa 647-SWCNT (red), and a merged image of the two. All scale bars are 10 μm. **b)** Intensity profiles of the two fluorophores along the dashed lines (cyan) in the overlay images. **c)** Histograms of Lysotracker Red intensity from 751 endolysosomal organelles that contained Alexa 647-SWCNT emission and 379 endolysosomal organelles that did not.

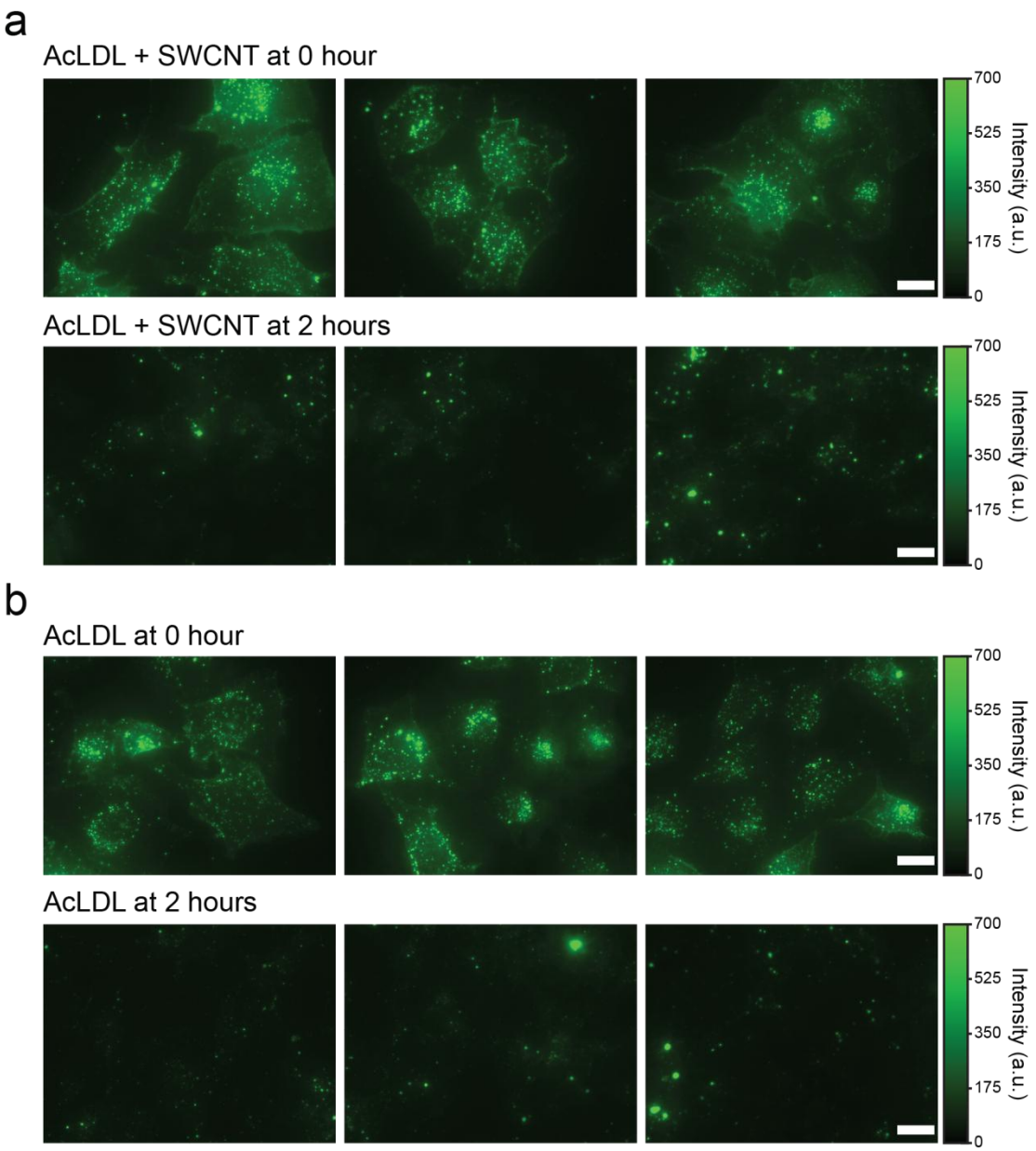

Figure S22: Acetylated-LDL (AcLDL) hydrolysis in U2OS-SRA cells. **a)** Representative epifluorescence images of Alexa 488-AcLDL (green) in U2OS cells, at 0 and 2 hours after the addition of AcLDL. Cells were treated with 1 mg/L of DNA-SWCNT for 30 minutes, before incubation in fresh media for an additional 90 minutes. Scale bar is 10 µm. **b)** Representative epifluorescence images of Alexa 488-AcLDL (green) in control U2OS cells, at 0 and 2 hours after the addition of acetylated LDL. Scale bar = 10 µm.

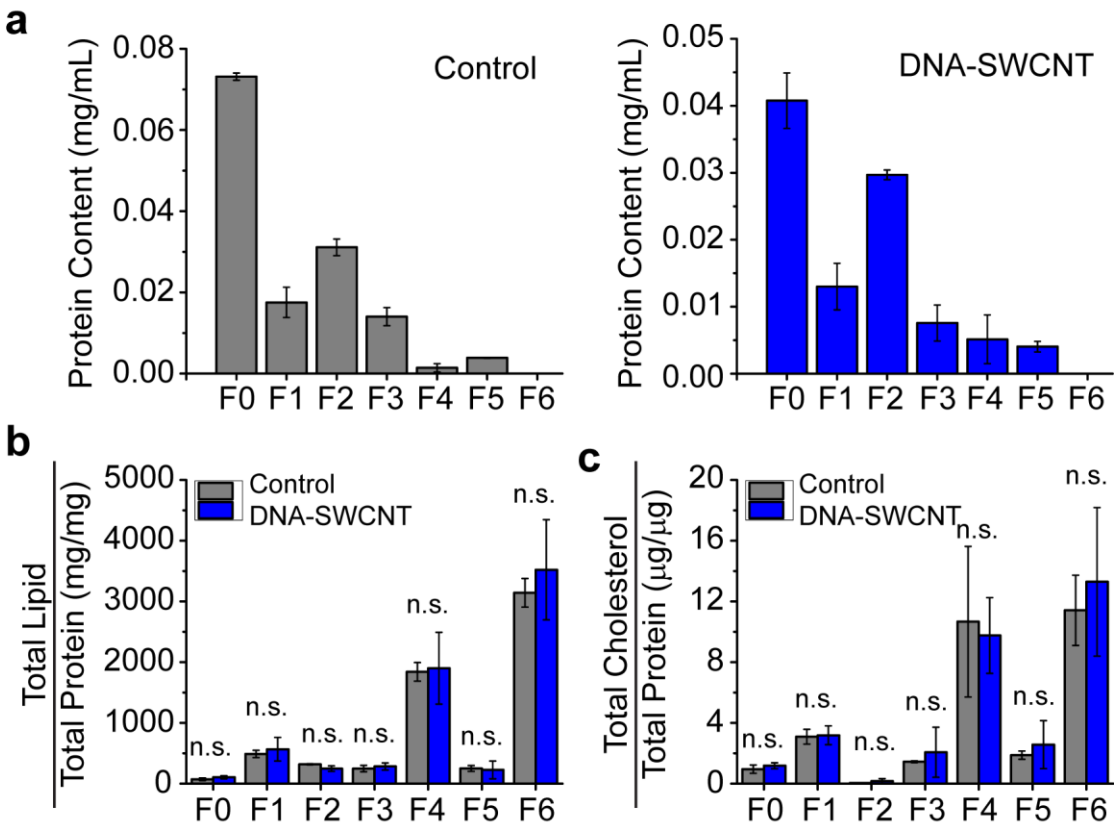

Figure S23: Cell fractionation and lipid biochemical assays. **a)** Total protein content measured in (left) fractionated RAW 264.7 macrophages, and (right) fractionated RAW 264.7 macrophages after treatment with 1 mg/L DNA-SWCNT complexes for 6 hours. **b)** Total lipid content of cell fractions, normalized by the total protein content of each fraction. **c)** Total cholesterol, normalized by the total protein content of each fraction. Error bars are standard deviation from 3 technical replicates. Fractions were compared using a one-way ANOVA with Sidak's multiple comparison test.

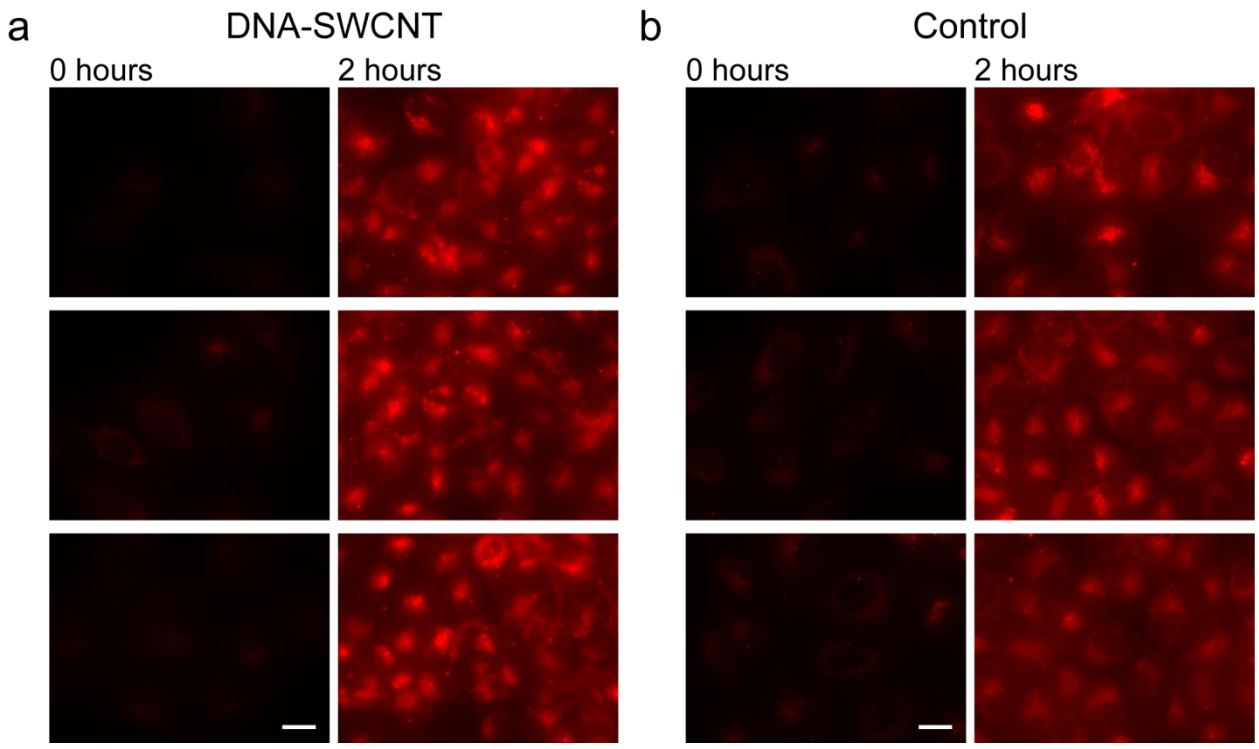

Figure S24: Free cholesterol efflux and formation of cytosolic lipid droplets in U2OS-SRA cells. Representative images of LipidTox Red Neutral Lipid Stain (red) in U2OS cells, at 0 and 2 hours after the addition of acetylated LDL, in cells containing **a)** 1 mg/L DNA-SWCNT and **b)** control cells. Scale bar = 10 µm. Images are set to the same contrast.

Effect of DNA-SWCNT on Cellular Cholesterol Storage:

As excess free cholesterol (FC) within cells can result in toxicity, FC is re-esterified into cholesteryl esters (CE) and stored as lipid droplets in the cytoplasm.[7] In the previous experiment (Figure 4 main text, S22), we had induced excess FC accumulation by incubating U2OS-SRA cells with 50 µg/mL acetylated LDL. In control cells and U2OS-SRA cells treated with 1 mg/L of Alexa 647-labeled nanotubes for 30 minutes, we stained the cells with LipidTox Red Neutral Lipid Stain. An increase in the neutral lipid content, apparent as the dramatic increase in LipidTox Red intensity (Figure S24), indicated the formation of lipid droplets in both control cells and those containing nanotubes, indicating that DNA-SWCNT did not prevent the digestion of acetylated LDL, nor the efflux and storage of free cholesterol.

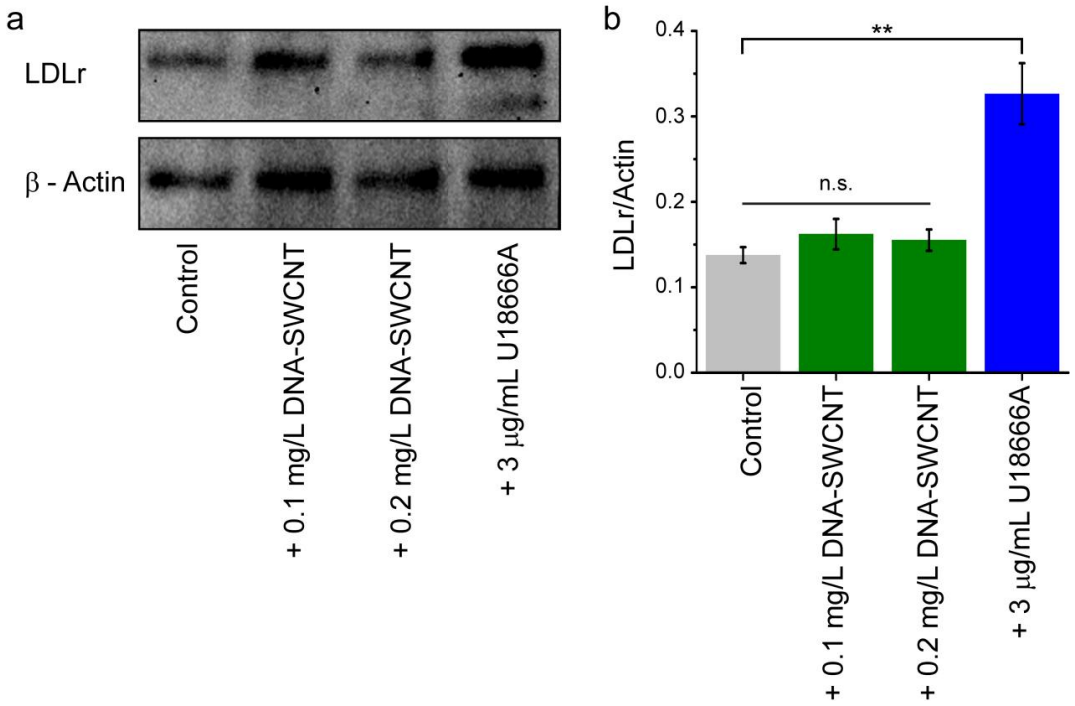

Figure S25: LDL receptor (LDLr) expression in RAW 264.7 macrophages. **a)** Western blots against LDLr of cells incubated with 0 (control), 0.1 and 0.2 mg/L DNA-nanotube complexes (DNA-SWCNT), and cells treated with 3 µg/mL U18666A. β-actin was used as the loading control. **b)** Quantification of band volumes, normalized to the β-actin band, compared using Dunnett's multiple comparison test, ** = $p < 0.01$. Error bars denote standard error of the mean from two technical replicates.

Effect of DNA-SWCNTs on Low Density Lipoprotein Receptor Expression:

Low-density lipoprotein is processed in the lysosomes *via* the sequential action of multiple acid hydrolases, including enzymes that digest the protein component of LDL, and lysosomal acid lipase, which hydrolyzes cholesteryl esters into free cholesterol (FC). Subsequently, proteins including Niemann-Pick C 1 and 2 transport the FC out of the lysosome, and the efflux of FC transcriptionally regulates the LDL receptor (LDLr) gene.[8] To test whether our reporter affected the activity of these proteins and thus decreased the free cholesterol efflux from the lysosomes, we performed a western blot for the LDL receptor in cells incubated with the DNA-nanotube complexes (DNA-SWCNT). As a positive control, we treated the cells with U18666A, a small molecule inhibitor of NPC-1,[9] which results in upregulation of the LDL receptor.[10]
Western blots (Figure S25) of LDLr in cells treated with DNA-nanotube complexes (DNA-SWCNT) indicate that nanotubes induced no differences in the LDLr expression levels, including at 0.2 mg/L (the working concentration of the reporter in the manuscript Figure S25). In contrast, a 3-fold increase in LDLr expression was observed in cells treated with 3 µg/mL U18666A. These data suggest that the LDL hydrolysis and lipoprotein-derived free cholesterol

efflux through the lysosome is not measurably perturbed by the presence of the reporter within the lysosomes.

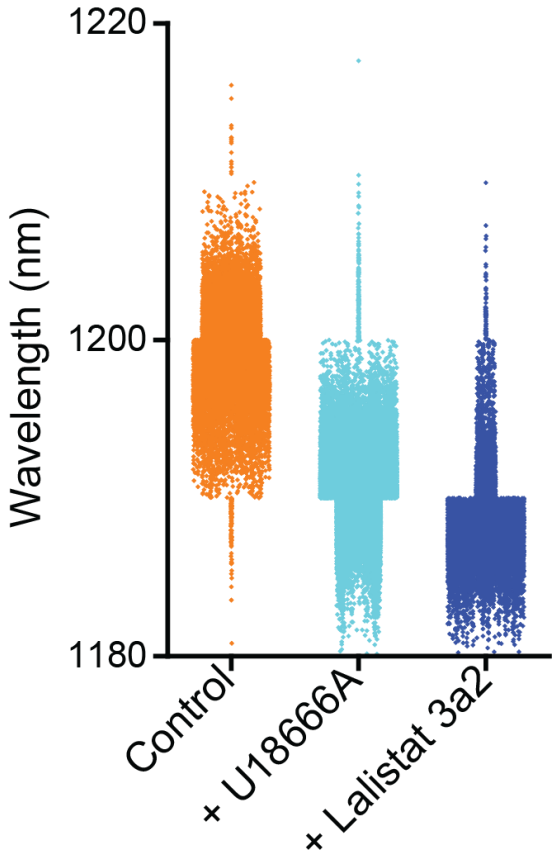

Figure S26: Point graph of emission wavelengths of all pixels represented in Figure 5c of the main text.

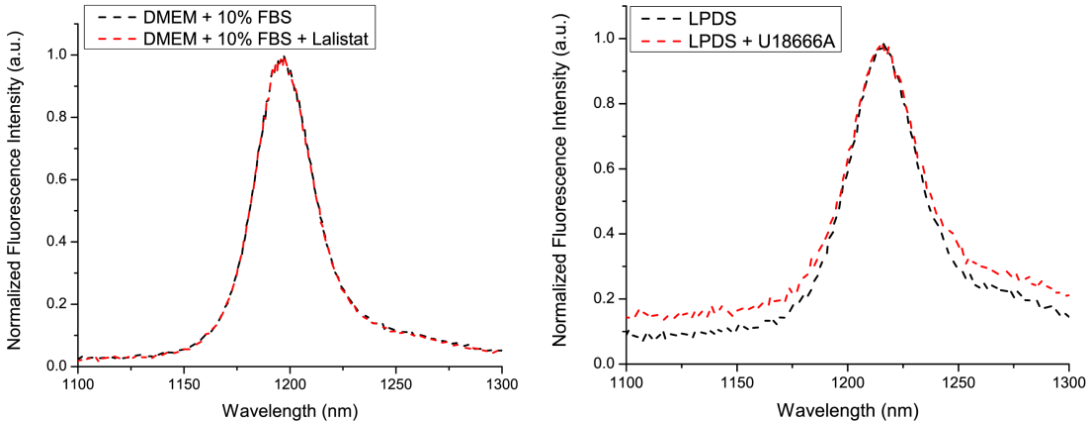

Figure S27: Effect of U18666A and Lalistat 3a2 on ss$(GT)_6$-(8,6) emission. Spectra of 0.2 mg/L ss$(GT)_6$-(8,6) complexes in media containing 10 µM Lalistat 3a2 (left), and media containing 3 µg/mL of U18666A (right). LPDS = Lipoprotein depleted serum.

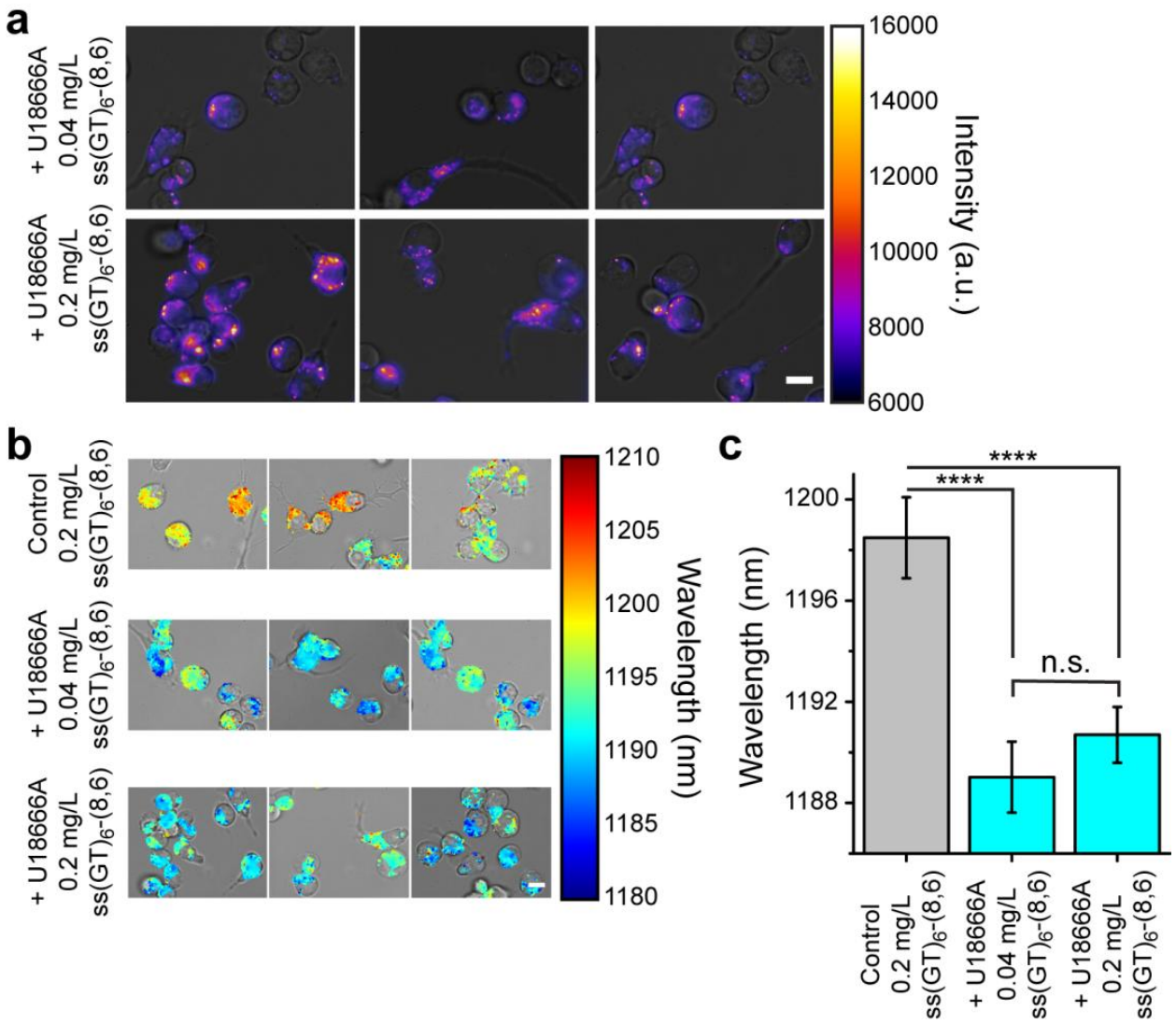

Figure S28: Effect of ss(GT)$_6$-(8,6) concentration on nanotube emission response to lipid accumulation. **a)** Broadband near-IR emission from ss(GT)$_6$-(8,6) complexes in RAW 264.7 macrophages introduced after 6 hours of incubation with 3 µg/mL U18666A in media. **b)** Hyperspectral images of the ss(GT)$_6$-(8,6) emission in the conditions described in panel a, as well as a control incubated without U18666A. **c)** Plots of the mean center wavelength of the emissive pixels from the hyperspectral data. Significance was calculated using a one-way ANOVA with Tukey's post test, n = 5 technical replicates. Error bars are standard deviation. **** = $p < 0.0001$. Scale bars = 10 µm.

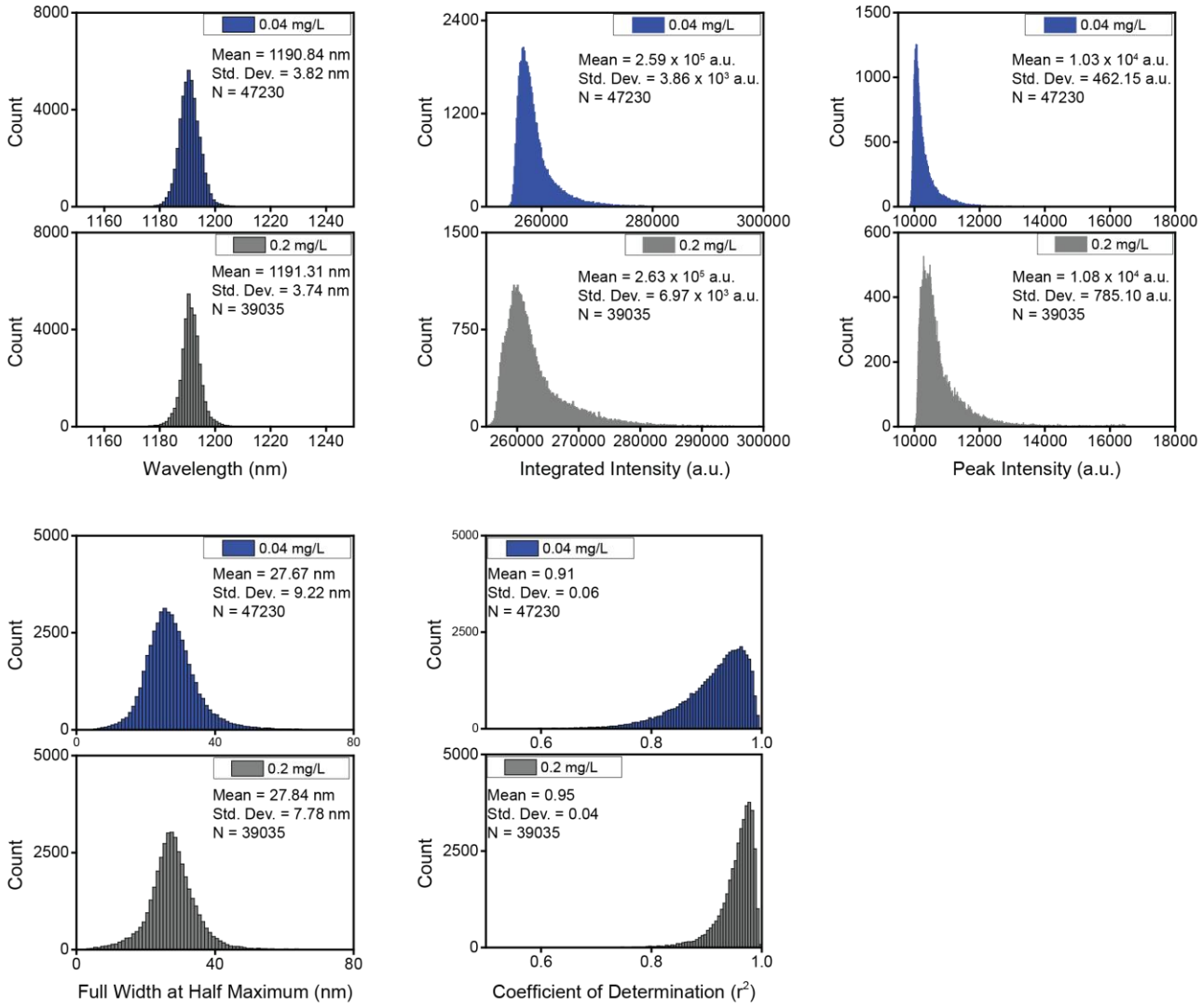

Figure S29: Effect of ss$(GT)_6$-(8,6) concentration on nanotube emission response. **a)** Histogram showing the effect of nanotube concentration on emission wavelength in RAW 264.7 macrophages treated with U18666A. **b)** Histogram showing the effect of nanotube concentration on the integrated intensity of nanotube containing pixels in RAW 264.7 macrophages treated with U18666A. **c)** Histogram showing the effect of nanotube concentration on the peak intensity of nanotube containing pixels in RAW 264.7 macrophages treated with U18666A. **d)** Histogram showing the effect of nanotube concentration on the emission bandwidth (full width at half maximum - FWHM) of nanotube-containing pixels in RAW 264.7 macrophages treated with U18666A. **e)** Histogram showing the effect of nanotube concentration on the coefficient of determination (r^2) calculated for fits of nanotube-containing pixels in RAW 264.7 macrophages treated with U18666A.

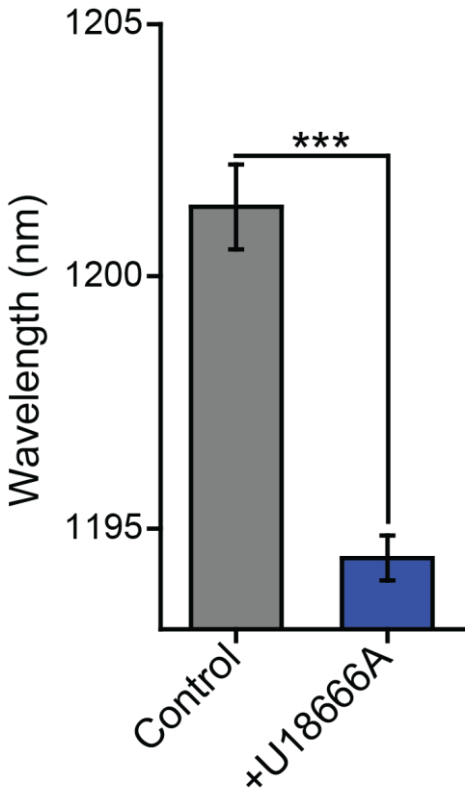

Figure S30: Validation of the reporter in mouse embryonic fibroblasts (MEFs). Average reporter emission wavelength in MEFs treated with 3 µg/mL U18666A for six hours and in untreated control MEFs. Error bars represent standard deviations from n = 3 replicates. Statistical significacne was determined with a t-test. *** = $p < 0.001$.

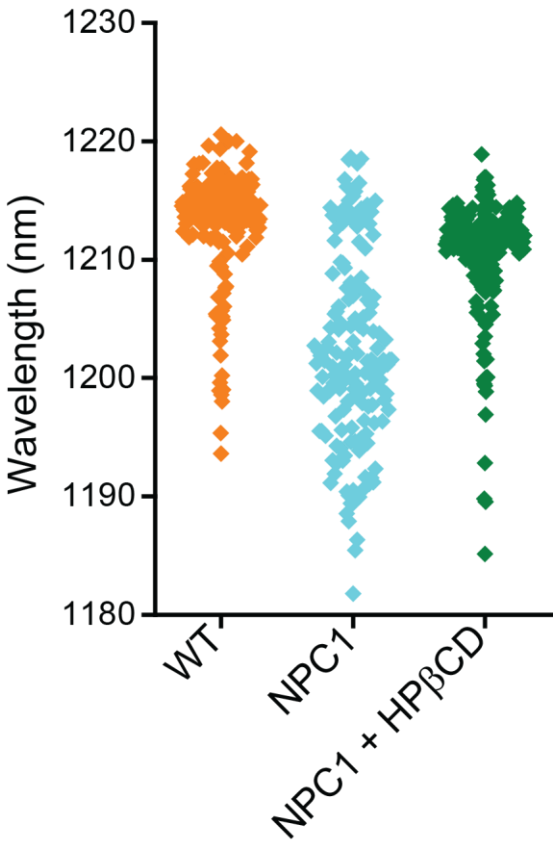

Figure S31: Point graph of emission wavelengths of all regions of interest (ROIs) represented in Figure 6b of the main text

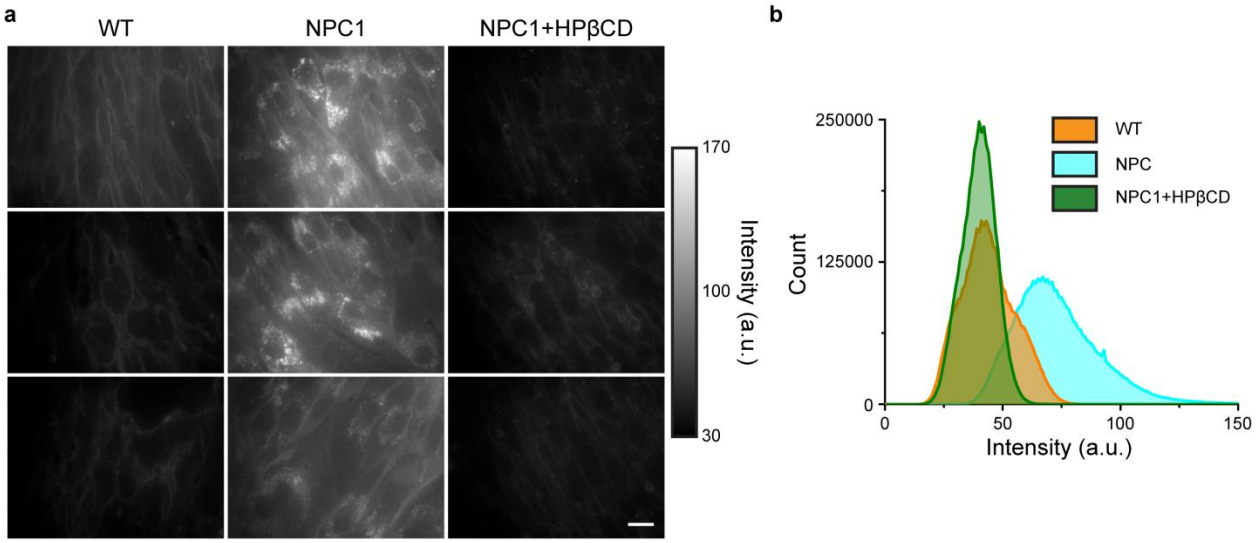

Figure S32: Filipin staining of NPC1 and WT human fibroblasts. **a)** Fluorescence images of wild-type fibroblasts, NPC patient-derived fibroblasts, and NPC patient-derived fibroblasts treated with hydroxypropyl-β-cyclodextrin (HPβCD) that were fixed, stained with filipin, and imaged using a 375/460 nm (Chroma 39000) filter set. Images were set to the same brightness and contrast. Scale bar = 20 μm. **b)** Histograms of pixel intensity for the same three conditions.

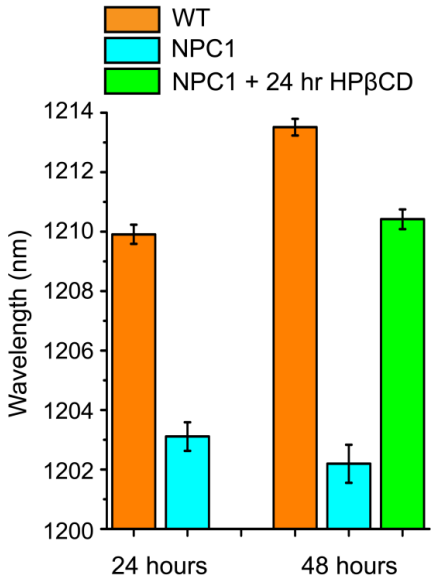

Figure S33: Reporter response in NPC1 human fibroblasts after pre-treatment with hydroxypropyl-β-cyclodextrin (HPβCD). Emission center wavelength of the reporter in wild-type (WT) fibroblasts, NPC patient-derived fibroblasts, and NPC patient-derived fibroblasts treated with HPβCD before introducing the reporter. Error bars represent standard error of the mean from n = 3 technical replicates.

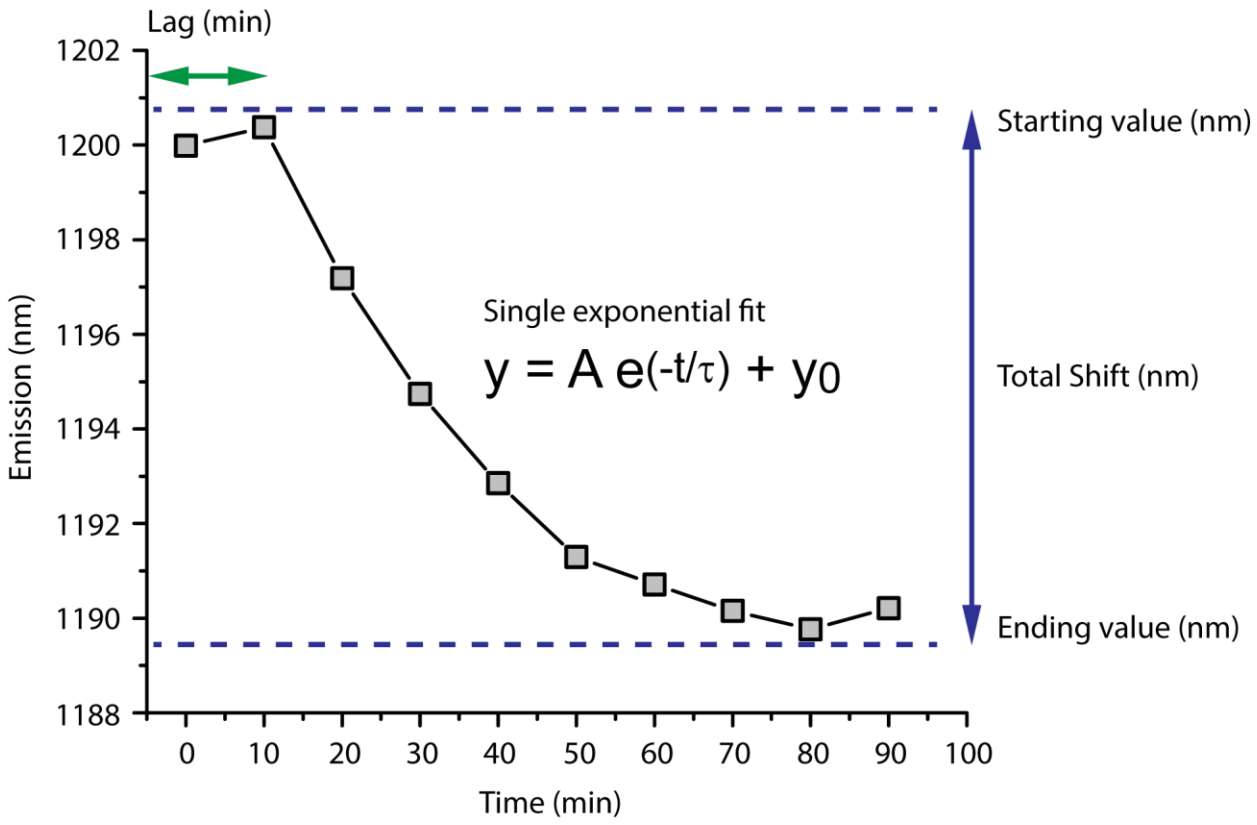

Figure S34: Fitting single-cell lipid accumulation trajectories. The mean of the reporter response trajectories upon addition of AcLDL to RAW 264.7 macrophages was fit with a single exponential function. For each cell, the lag time (min), starting wavelength (nm), ending wavelength (nm), and total shift (nm) were quantified and used for further analysis. Data were fit to a single exponential decay with pre-exponential constant, A, time constant, τ, and y-offset, $y_{0.}$

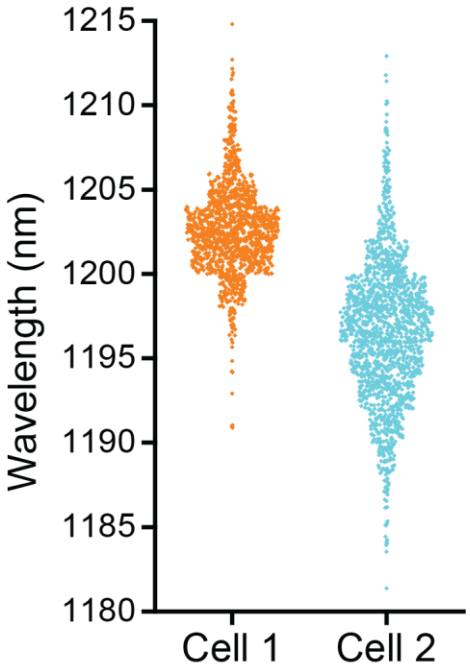

Figure S35: Point graph of emission wavelengths of all pixels represented in Figure 8c of the main text.

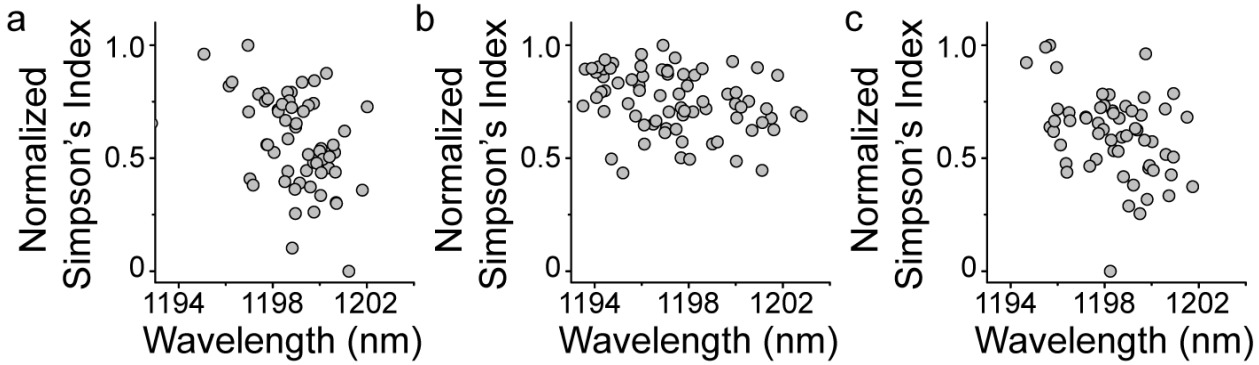

Figure S36: Scatter-plot of the normalized Simpson's Index against the mean emission wavelength per cell (differentiated under the action of colony stimulating factor-1 (CSF-1) for 3 days), for bone marrow derived monocytes from 3 mice in addition to the one used in Figure 8 of the manuscript. Spearman correlations were **(a)** -0.44, **(b)** -0.38 and **(c)** -0.36, with $p < 0.001$.

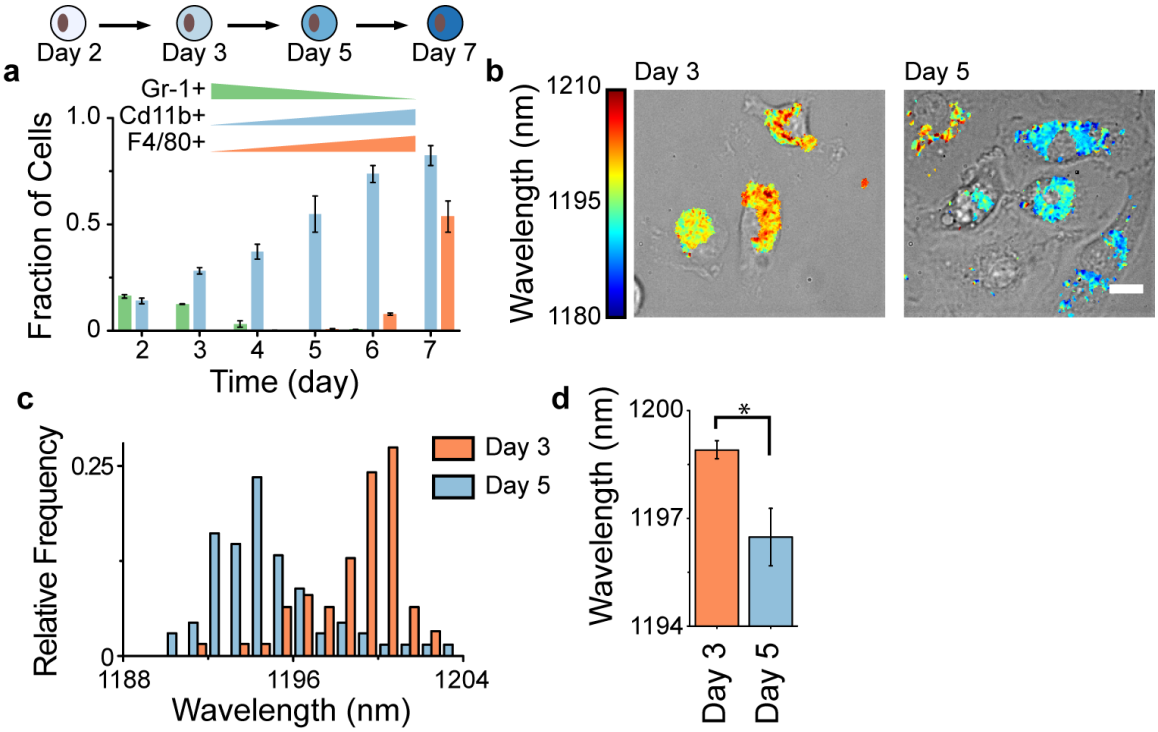

Figure S37: Changes in the endolysosomal lipid content in maturing bone marrow-derived monocytes. **a)** Temporal changes in expression of the macrophage markers Cd11b and F4/80 and monocyte/granulocyte marker Gr-1 in murine bone marrow-derived cells in the presence of CSF-1. Error bars denote standard deviations from n = 8 mice. **b)** Overlaid brightfield and hyperspectral images of the reporter in maturing bone marrow-derived cells at days 3 and 5 after harvesting. **c)** Histogram of the mean reporter emission wavelength, measured per cell, at days 3 and 5 after harvesting. **d)** Differences in the mean reporter emission wavelength from cells at days 3 and 5, from n = 4 mice. Values were compared using an unpaired t-test, * = $p < 0.05$. Scale bars = 10 µm.

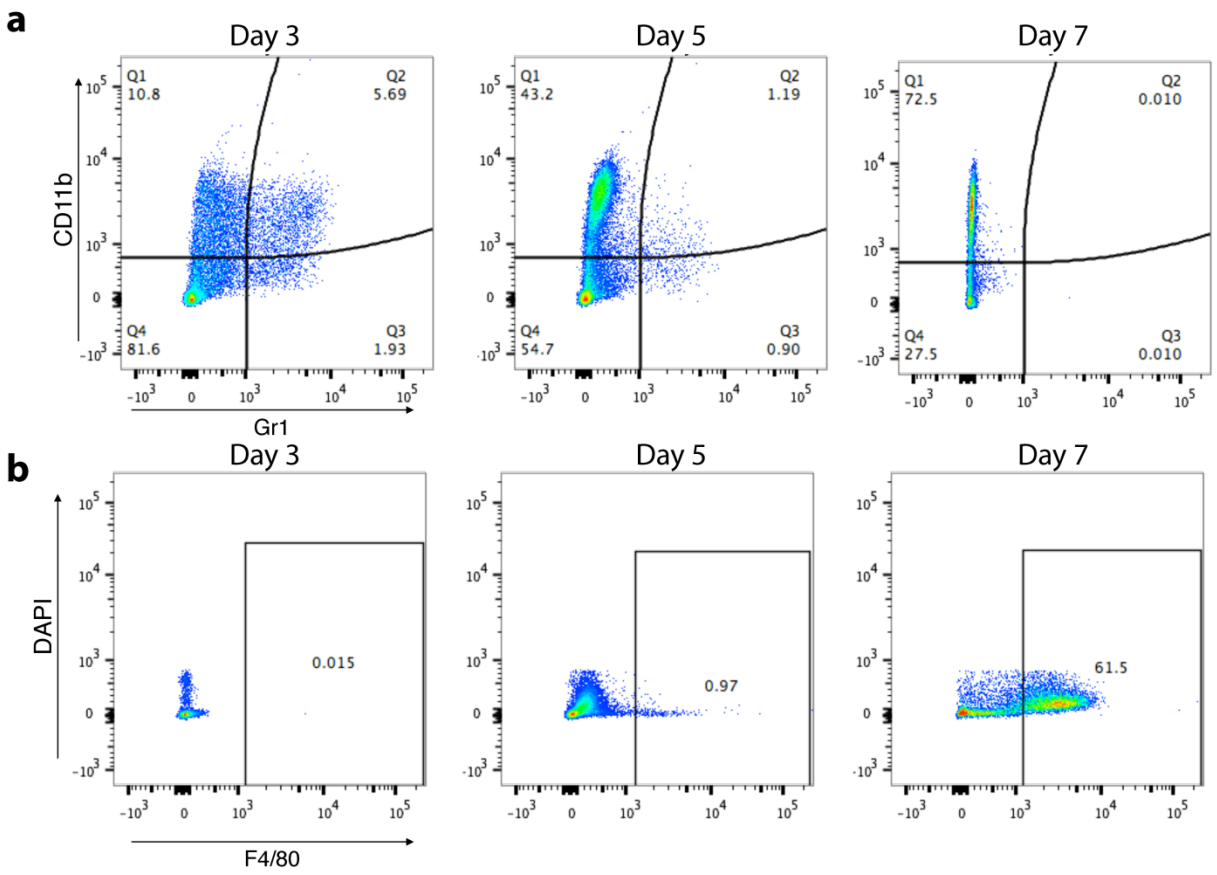

Figure S38: Flow cytometry analysis of bone marrow-derived monocyte differentiation. **a)** Monocytes cultured in CSF-1 media, assessed for the expression of monocytic/granulocytic marker Gr-1 (X axis) and the macrophage marker Cd11b (Y axis).
b) Macrophage marker F4/80, showing enrichment of the macrophage population.

<u>Detection of endolysosomal lipid accumulation in a non-pathological condition:</u>

As bone marrow derived monocytes differentiate into bone marrow derived macrophages (BMDMs) in the presence of colony stimulating factor 1 (CSF-1), they accumulate LDL derived cholesterol.[11,12] In order to determine if the developed reporter was capable of detecting non-pathological increases in endolysosomal lipid accumulation, we used the reporter to monitor endolysosomal lipid accumulation during the differentiation process. Bone marrow-derived monocytes, isolated from C57BL/6 mice, were cultured in the presence of CSF-1 for 7 days to induce differentiation into macrophages.[13] The differentiation process was verified by the increase in the fraction of cells expressing the macrophage markers Cd11b and F4/80, and a decrease in the fraction of cells expressing the monocytic/granulocytic marker Gr-1 (Figure S37,38).[14] Following incubation of the BMDMs with the reporter for 30 minutes, free reporter was rinsed away and the cells were incubated for an additional 6 hours in CSF-1 containing cell culture media. Endolysosomal lipid maps generated from BMDMs after 3 and 5 days of

maturation were strikingly different (Figure S37). As seen in the histogram of the mean reporter emission from individual cells, the reporter blue-shifted by approximately 5 nm between day 3 and day 5 of maturation (Figure S37), indicating that accumulation of lipids in the endolysosomal lumen accompanied the macrophage differentiation in this timeframe. We confirmed this finding in 4 separate animals with 10 technical replicates each (Figure S37).

Solvent	Dielectric (ε)	Mean emission wavelength (nm)	S.E.M.	Number of complexes
Air	1	1189.18	0.83	335
Butanol	18	1187.31	0.71	124
Propylene Glycol	32	1190.83	0.64	388
Glycerol	42.5	1189.75	0.39	232
Dimethyl sulfoxide (DMSO)	46.7	1195.96	0.25	398
Propylene Carbonate	64	1206.26	0.47	158
Water	80	1201.03	0.31	192

Table S1: Photoluminescence modulation of surface-bound ss$(GT)_6$-(8,6) nanotube complexes interrogated with solvents of varying dielectric constants.

References:

(1) Roxbury, D.; Jagota, A.; Mittal, J. Sequence-Specific Self-Stitching Motif of Short Single-Stranded DNA on a Single-Walled Carbon Nanotube. *J. Am. Chem. Soc.* **2011,** *133*, 13545–13550.

(2) Roxbury, D.; Mittal, J.; Jagota, A. Molecular-Basis of Single-Walled Carbon Nanotube Recognition by Single-Stranded DNA. *Nano Lett.* **2012,** *12*, 1464–1469.

(3) Sugita, Y.; Okamoto, Y. Replica-Exchange Molecular Dynamics Method for Protein Folding. *Chem. Phys. Lett.* **1999,** *314*, 141–151.

(4) Jorgensen, W. L.; Chandrasekhar, J.; Madura, J. D.; Impey, R. W.; Klein, M. L. Comparison of Simple Potential Functions for Simulating Liquid Water. *J. Chem. Phys.* **1983,** *79*, 926–935.

(5) Humphrey, W.; Dalke, A.; Schulten, K. VMD: Visual Molecular Dynamics. *J. Mol. Graph.* **1996,** *14*, 33–38.

(6) Costes, S. V.; Daelemans, D.; Cho, E. H.; Dobbin, Z.; Pavlakis, G.; Lockett, S. Automatic and Quantitative Measurement of Protein-Protein Colocalization in Live Cells. *Biophys. J.* **2004,** *86*, 3993–4003.

(7) Dubland, J. A.; Francis, G. A. Lysosomal Acid Lipase: At the Crossroads of Normal and Atherogenic Cholesterol Metabolism. *Front. Cell Dev. Biol.* **2015,** *3*. 1–11.

(8) Goldstein, J. L.; Brown, M. S. The LDL Receptor. *Arterioscl. Throm. Vas.* **2009,** *29*, 431–438.

(9) Lu, F.; Liang, Q.; Abi-Mosleh, L.; Das, A.; de Brabander, J. K.; Goldstein, J. L.; Brown, M. S. Identification of NPC1 as the Target of U18666A, an Inhibitor of Lysosomal Cholesterol Export and Ebola Infection. *eLife* **2015,** *4*. 1–16.
(10) Issandou, M.; Guillard, R. L.; Boullay, A. B.; Linhart, V.; Lopez-Perez, E. Up-Regulation of Low-Density Lipoprotein Receptor in Human Hepatocytes is Induced by Sequestration of Free Cholesterol in the Endosomal/Lysosomal Compartment. *Biochem. Pharmacol.* **2004,** *67*, 2281–2289.
(11) Anzinger, J.; Chang, J.; Xu, Q.; Buono, C.; Li, Y. F.; Leyva, F.; Park, B. C.; Greene, L.; Kruth, H. Native Low-Density Lipoprotein Uptake by Macrophage Colony-Stimulating Factor-Differentiated Human Macrophages is Mediated by Macropinocytosis and Micropinocytosis. *J. Immunol.* **2010,** *184*. 2022–2031.
(12) Zhao, B.; Li, Y. F.; Buono, C.; Waldo, S. W.; Jones, N. L.; Mori, M.; Kruth, H. S. Constitutive Receptor-Independent Low Density Lipoprotein Uptake and Cholesterol Accumulation by Macrophages Differentiated from Human Monocytes with Macrophage-Colony-Stimulating Factor (M-CSF). *J. Biol. Chem.* **2006,** *281*, 15757–15762.
(13) Pyonteck, S. M.; Akkari, L.; Schuhmacher, A. J.; Bowman, R. L.; Sevenich, L.; Quail, D. F.; Olson, O. C.; Quick, M. L.; Huse, J. T.; Teijeiro, V.; *et al.* CSF-1R Inhibition Alters Macrophage Polarization and Blocks Glioma Progression. *Nat. Med.* **2013,** *19*, 1264–1272.
(14) Akkari, L.; Gocheva, V.; Kester, J. C.; Hunter, K. E.; Quick, M. L.; Sevenich, L.; Wang, H. W.; Peters, C.; Tang, L. H.; Klimstra, D. S.; *et al.* Distinct Functions of Macrophage-Derived and Cancer Cell-Derived Cathepsin Z Combine to Promote Tumor Malignancy *via* Interactions with the Extracellular Matrix. *Genes Dev.* **2014,** *28*, 2134–2150.